MASTERARBEIT / MASTER'S THESIS

Titel der Masterarbeit / Title of the Master's Thesis

Evolution of Earth's Oxygen, Nitrogen, and Carbon Polar Outflow in the Archean Eon

verfasst von / submitted by

Natalie Grasser, BSc

angestrebter akademischer Grad / in partial fulfilment of the requirements for the degree of

Master of Science (MSc)

Wien, 2023 / Vienna, 2023

Studienkennzahl lt. Studienblatt / degree programme code as it appears on the student record sheet:	A 066 861
Studienrichtung lt. Studienblatt / degree programme as it appears on the student record sheet:	Masterstudium Astronomie
Betreut von / Supervisor:	Dr. Kristina Kislyakova

Abstract

The habitability of Earth significantly depends on the evolution of its atmospheric properties, which are strongly influenced by escape processes. Polar outflow, which encompasses the atmospheric escape of ions through the open field lines of the Earth's magnetosphere, is the dominant escape process for modern Earth and likely played a significant role in Earth's early history as well. In this article, we investigate the evolution of Earth's polar outflow during the Archean eon 3-4 gigayears (Ga) ago for an N_2-CO_2 atmosphere. For this, we use a kinetic direct simulation Monte Carlo (DSMC) particle code to simulate the interactions between the solar wind and the Earth's upper atmosphere. We explore the effects of different CO_2 mixing ratios (10%,25%,50%,75%,99%) on the polar outflow escape rates of oxygen, nitrogen and carbon. Using the ion production rates as a proxy for polar outflow, our results indicate that during the time 3.6-4.0 Ga ago, a CO_2 mixing ratio larger than 25% may have been necessary to avoid excessive escape via polar outflow. Close to 4 Ga ago, even 50% CO_2 may have been necessary due to the stronger solar winds. Our results align with other studies also suggesting a similarly high CO_2 mixing ratio in the early Archean.

Die Habitabilität der Erde hängt wesentlich von der Entwicklung ihrer atmosphärischen Eigenschaften ab, die stark von atmosphärischen Verlustprozessen beeinflusst werden. Der polare Ausfluss, der das atmosphärische Entweichen von Ionen durch die offenen Feldlinien der Erdmagnetosphäre umfasst, ist der dominierende Verlustprozess der modernen Erdatmosphäre und spielte wahrscheinlich auch in der Frühgeschichte der Erde eine bedeutende Rolle. In diesem Artikel untersuchen wir die Entwicklung des polaren Ausflusses der Erde während des Archaischen Äons vor 3-4 Gigajahren (Ga) für eine N_2-CO_2-Atmosphäre. Dazu verwenden wir einen kinetischen Direct Simulation Monte Carlo (DSMC)-Partikelcode, um die Wechselwirkungen zwischen dem Sonnenwind und der oberen Erdatmosphäre zu simulieren. Wir untersuchen die Auswirkungen verschiedener atmosphärischen CO_2 Verhältnissen (10%,25%,50%,75%,99%) auf die polaren Ausströmungsraten von Sauerstoff, Stickstoff und Kohlenstoff. Unter Verwendung der Ionenproduktionsraten als Näherungswert für den polaren Ausfluss deuten unsere Ergebnisse darauf hin, dass während der Zeit vor 3.6-4.0 Ga ein CO_2 Verhältnis von mehr als 25% notwendig gewesen sein könnte, um übermäßige atmosphärische Verluste über den polaren Ausfluss zu vermeiden. Vor etwa 4Ga könnten aufgrund der stärkeren Sonnenwinde sogar 50% CO_2 notwendig gewesen sein. Unsere Ergebnisse stimmen mit anderen Studien überein, die ebenfalls auf ein ähnlich hohes CO_2 Verhältnis im frühen Archaikum hindeuten.

Contents

1 Introduction **2**

2 Methods and input parameters **8**

2.1 Input data 8

2.2 Direct Simulation Monte Carlo code 14

3 Evolution of Earth's Oxygen, Nitrogen, and Carbon Polar Outflow in the Archean Eon **17**

Publication details 17

3.1 Introduction 18

3.2 Methods and input parameters 19

3.2.1 Input data 19

3.2.2 Direct Simulation Monte Carlo code 21

3.3 Results and discussion 23

3.4 Conclusions 27

4 Conclusions **30**

Bibliography **32**

Chapter 1

Introduction

So far, Earth is the only planet known to host life. Currently, 5338 planets outside of our solar system, so-called exoplanets, have been discovered[1], yet very little is known about most of them due to observational limitations. Searching for a planet with habitable conditions is an exciting prospect that is gradually starting to come within reach due to the rapid improvements in technology. Although not all habitable environments will result in the emergence of life, habitable conditions are a necessary prerequisite for life to evolve. However, we have yet to comprehend how our own planet became habitable in the first place. In order to understand what conditions favor the development of life, it is crucial to understand the conditions that were present on Earth back when life first emerged 4 billion years (Ga) ago [Javaux, 2019], in particular in regards to its atmosphere.

Although the Earth has been habitable for most of its history, it has undergone significant changes in its geological conditions and atmosphere throughout its lifetime. The habitable conditions that we live in today are certainly not the same as those that were present during the Archean eon 2.5-4 Ga ago, which encompasses one third of Earth's history. It is known that Earth's early atmosphere contained a lot more carbon dioxide and methane, yet hardly any oxygen [Catling and Zahnle, 2020]. However, due to limited data, the atmospheric conditions present on Earth when life first emerged are not very precisely constrained and require further studies.

The habitability of a planet depends on a complex interplay of many different factors, one of them being the presence of liquid water. Water is often referred to as a universal solvent, since it can dissolve more substances than any other liquid. In fact, it is considered the best solvent for life to emerge and evolve in [Lammer et al., 2009]. Furthermore, it consists of two very common elements and has been found abundantly in space, from cold dense molecular clouds to hot stellar atmospheres [Cernicharo and Crovisier, 2005]. Around every star exists a circular region in which liquid water could exist on the surface of a rocky planet similar to Earth. This region is called the habitable zone (HZ), where it is neither too hot, nor too cold for liquid water and life to exist. The distance of this region depends on the spectral type of the host star and their evolutionary stage. The hotter the star, the further away lies their habitable zone. As stars become larger as they evolve, the habitable zone also moves further out over time. Considering less conservative limits, the habitable zone around our Sun

[1] https://exoplanetarchive.ipac.caltech.edu/, accessed: April 27, 2023

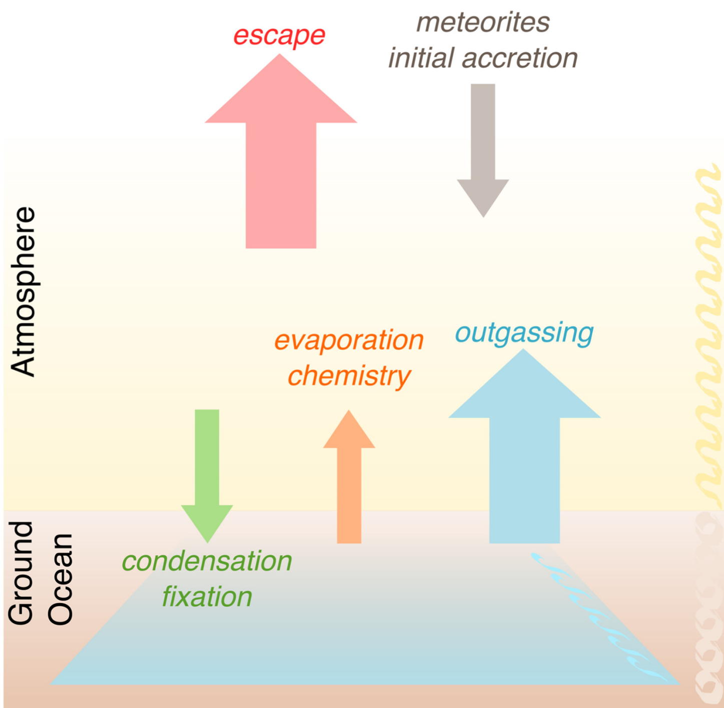

Figure 1.1: The factors that influence the creation, destruction and composition of an atmosphere [Gronoff et al., 2020].

is thought to be at 0.75–1.77 AU (astronomical unit), where 1 AU = 150 million km, which is the distance between the Earth and the Sun [Ramirez, 2018].

However, the definition of the habitable zone does not take into account the various other factors required to make a planet habitable, such as the presence and maintenance of an atmosphere. An atmosphere is essential for habitability, since it provides a sufficiently high temperature and pressure to maintain liquid water on a planet's surface [e.g., Huang, 1959, Kasting et al., 1993, Kopparapu et al., 2013].

On one hand, the creation of an atmosphere depends on processes like initial accretion of volatiles from the protostellar nebula, meteorites, outgassing from the planet's interior through volcanic eruptions, surface interactions such as evaporation and chemical reactions. On the other hand, the destruction of an atmosphere is influenced by condensation, fixation and atmospheric escape. These processes also determine the composition of the atmosphere and are summarized in Figure 1.1. To produce a habitable atmosphere, there must be a continuous stable balance between the processes that add and remove atmospheric particles [Gronoff et al., 2020].

The evolution of a planet's atmosphere is to a large extent governed by its escape to space, and many factors play a role including the physical characteristics of a planet, dynamics of its orbit and rotation, and outgassing history [Van Hoolst et al., 2019]. The evolution of the short-wavelength solar radiation and wind, as well as the evolution of the atmosphere's composition, are factors that strongly affect the extent of atmospheric escape (e.g., Chamberlain 1963, Chamberlain and Hunten 1987, Gronoff et al. 2020). Some atmospheric constituents are capable of reducing the escape rates, while there are also constituents that are more likely to escape themselves, in particular lighter particles and isotopes.

Atmospheric escape can be divided into thermal and non-thermal processes. Thermal escape processes arise from the heating and hence accelerating of the upper atmosphere particles and are heavily influenced by the host star's X-ray and extreme ultraviolet radiation [together XUV; wavelength range 1–400 nm, as in Johnstone et al., 2018, 2021]. There are two categories of thermal escape that depend on the altitude at which they are taking place, namely Jeans escape and hydrodynamical escape. In this context, the exobase radius is an important parameter. The exobase radius is defined as the altitude at which the atmosphere transitions from being collisional to collisionless. Hydrodynamical escape occurs below the exobase, where the atmosphere is denser and therefore collisional. In this region, thermal acceleration can cause atmospheric particles to escape as a flow of continuous fluid and also drag other particles along with them. On the other hand, Jeans escape occurs above the exobase in the so-called exosphere, which is a part of the upper atmosphere that is very thin and can be considered collisionless. The temperatures of the atmospheric particles are distributed according to a Maxwellian distribution. Jeans escape occurs when individual particles in the high-energy tail of the Maxwellian distribution escape to space [Gronoff et al., 2020]. The heating of the upper atmosphere through the solar XUV radiation also causes a planetary atmosphere to expand. This further reduces the planet's gravitational force on the particles due to them being further away from the planet, which also enhances escape.

In contrast to thermal escape, non-thermal escape processes encompass various other complex interactions between the stellar wind and atmospheric particles. One of these is photochemical escape, which occurs when chemical reactions provide enough energy for the escape of atmospheric particles. This can happen through ion recombination or molecular photodissociation, which release kinetic energy that can cause particles to escape. Charge exchange is another relevant process, which occurs when an ion exchanges its charge with an atmospheric particle. Through this process, the ion then becomes an energetic neutral atom (ENA) that can access thermosphere and increases heating through the transfer of kinetic energy. Charge exchange can take place with solar wind ions, ions trapped in the planet's magnetosphere, or precipitating ions. Through the process of ion pickup, the solar wind can pick up ions from the ionosphere, which is the ionized part of the Earth's upper atmosphere. Ion sputtering is another non-thermal escape process through which accelerated ions from the ionosphere translate their kinetic energy. The non-thermal escape process that is the focus of this work is polar outflow, which occurs when ions escape along the open field lines of a planet's magnetosphere. This ion upward wind is created through ambipolar diffusion, when the lighter electrons diffuse upwards from the heavier ions, creating an electric field that accelerates ions [e.g., Lammer 2013, Gronoff et al. 2020]. The various escape processes are summarized in Figure 1.2 from Gronoff et al. [2020]. Processes such as trapped ion charge exchange and polar outflow can only occur for planets with a magnetic field, while other processes can occur for both magnetized and unmagnetized planets.

The escape processes described above are heavily influenced by the stellar short-wavelength radiation and wind. These parameters are also variable over time and evolve together with the star. Studies have shown that the Sun's XUV flux and wind have evolved dramatically and were significantly higher in Earth's early history [e.g., Güdel, 2007, Johnstone et al., 2015, Tu et al., 2015], which enhanced atmospheric escape from the planet [e.g., Lichtenegger et al., 2010, Johnstone et al., 2021]. According to Tian et al. [2008a,b], modern Earth's N_2-O_2-

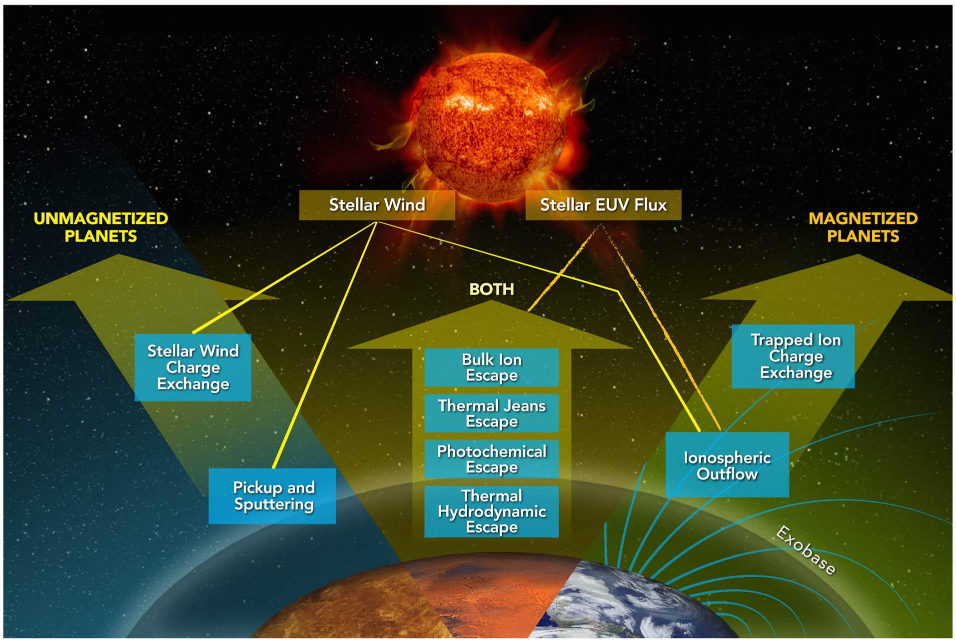

Figure 1.2: Thermal and non-thermal atmospheric escape processes, depicted at the typical altitudes and conditions at which they take place [Gronoff et al., 2020].

dominated atmosphere would rapidly escape thermally if exposed to solar radiation as strong as it was during the early Archean eon (4-2.4 Ga), while a recent model by Nakayama et al. [2022] yields contrasting results on the thermospheric structure. However, it is clear that the Earth's atmospheric composition was significantly different in its early history in order for it to have survived such harsh conditions and still remain habitable. An atmosphere stable against atmospheric erosion is in agreement with significant geological evidence on the presence of liquid water and life during the Archean eon [Javaux, 2019].

Figure 1.3 from Catling and Zahnle [2020] illustrates the evolution of the Earth's atmospheric composition over its lifetime by portraying the partial pressure of molecular nitrogen (N_2), molecular oxygen (O_2), carbon dioxide (CO_2), and methane (CH_4). While modern Earth's atmosphere consists of 78% N_2 and 21% O_2, one can see that this has not always been the case. The atmospheric composition prior to the Great Oxygenation Event (GOE) at about 2.5 Ga ago was significantly different than at present-day with no appreciable O_2 [e.g., Lyons et al., 2014, Stüeken et al., 2020]. In fact, Earth's atmosphere in its early history presumably consisted primarily of N_2 and CO_2, including a higher but still low level of methane. Geochemical measurements of paleosols, which are ancient soils that were preserved under sediments, suggest that the CO_2 partial pressure may have been significantly higher than in the current atmosphere [e.g., Kanzaki and Murakami 2015].

Higher levels of CO_2 in Earth's early history are beneficial in two ways. For one, CO_2 acts as a coolant in the upper atmosphere by radiating infrared (IR) back into space. The ability to absorb and re-emit IR radiation also causes CO_2 to heat the lower regions of Earth's atmosphere, yet this process produces the opposite effect in the Earth's upper atmosphere due to most of the re-emitted IR being lost to space instead of going back to the planet. Therefore, a higher mixing ratio of this gas leads to lower atmospheric thermal [e.g., Johnstone et al., 2021] and non-thermal escape rates [e.g., Lichtenegger et al., 2010] through cooling the upper

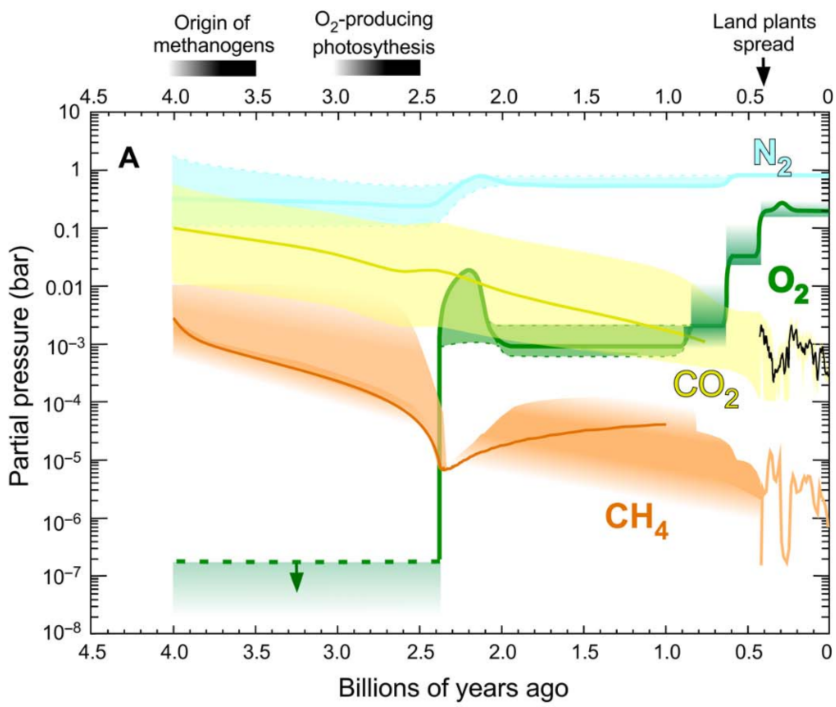

Figure 1.3: Evolution of the Earth's atmospheric composition over its lifetime, depicting the partial pressure of molecular nitrogen (N_2), molecular oxygen (O_2), carbon dioxide (CO_2), and methane (CH_4)[Catling and Zahnle, 2020].

atmosphere.

Another point is the so-called Faint Young Sun (FYS) paradox. About 3-4 Ga ago, the Sun was 30% fainter than it is today [Claire et al., 2012], which would result in the Earth being frozen and having no liquid water or life on its surface. However, several studies suggest the presence of an active hydrological cycle and mild temperatures during that period [e.g., Lammer et al., 2009, Mojzsis et al., 2001, Knauth and Lowe, 2003]. Higher levels of greenhouse gases like CO_2 would solve the FYS paradox by heating the lower regions of Earth's atmosphere. Johnstone et al. [2021] have shown that a nitrogen-dominated atmosphere (at least without appreciable amounts of O_2) prior to the GOE should have had a CO_2 mixing ratio of at least 40% at the start of the Archean to prevent rapid thermal escape of the atmosphere due to the young Sun's XUV radiation. This CO_2 mixing ratio would also be high enough to resolve the FYS paradox [e.g., Feulner, 2012, Charnay et al., 2020]. However, this study did not take into account non-thermal escape processes.

Some non-thermal ion loss processes, including polar outflow, are governed by a planet's intrinsic magnetic field. Polar outflow, also referred to as polar wind, ion outflow or ionospheric outflow, occurs when charged atmospheric particles escape along the field lines of a planet's magnetosphere [e.g., Gronoff et al., 2020]. A planetary magnetosphere can, on one hand, protect an atmosphere from stellar wind erosion. On the other hand, ions can escape from the open field line bundles if sufficient energy and momentum exchange occurs between the solar wind and atmospheric particles [e.g., Blackman and Tarduno, 2018]. On present-day Earth, atmospheric escape is indeed dominated by polar outflow from the open field line bundle [e.g., Gunell et al., 2018]. Since Earth has had its magnetic field since its early history, polar outflow has likely been the dominant escape process back until at least the GOE [Kislyakova et al., 2020]. Whether polar outflow was dominating atmospheric losses during the Archean eon is yet unknown. However, it is known that Earth's magnetic field has existed as early as 4.2 Ga, even though its field strength was likely weaker during the Archean eon [Tarduno et al., 2015, 2020].

The extent of atmospheric escape through polar outflow in the Archean eon has not yet been studied quantitatively, although it is likely to have had a significant contribution to the atmospheric escape of early Earth. Kislyakova et al. [2020] quantitatively investigated the evolution of the Earth's polar outflow from mid-Archean to the present time. In this follow-up study, I collaborated with Kristina Kislyakova, Manuel Scherf, Helmut Lammer, and Gwenaël van Looveren to study the Earth's polar outflow during the Archean eon. We investigate the evolution of the polar ion outflow rates from early Earth (3-4 Ga) for N_2-CO_2-atmospheres with different CO_2 mixing ratios (99%, 75%, 50%, 25%, 10%) considering the evolving solar wind, Earth's paleomagnetosphere and atmospheric composition. We assume that the young Sun evolved as a slow rotator [Tu et al., 2015], because otherwise Earth's atmosphere would have likely been lost due to thermal escape [Johnstone et al., 2021]. For this purpose, we employ the same kinetic Direct Simulation Monte Carlo (DSMC) particle model as in Kislyakova et al. [2020], through which the effects of different CO_2 mixing ratios on atmosphere maintenance can be explored. The article was submitted to Earth and Planetary Science Letters (EPSL) on April 13, 2023, and it is currently under review.

Chapter 2

Methods and input parameters

2.1 Input data

In order to simulate the Earth's atmosphere under Archean-like conditions, we need the values of several key parameters that influence the escape in a period of 3-4 Ga ago and for the different CO_2 mixing ratios that we want to investigate. These parameters are:

- Atmosphere properties:
  - Inner boundary: altitude, temperature
  - N, O, C: densities, ionisation rates
- Solar wind: density, temperature, velocity
- Shape of the magnetosphere:
  - Radius of the subsolar point
  - Magnetosphere width

As input data for the simulation, we adopt the upper atmosphere densities, temperatures and ionization rates determined for early Earth with the Kompot Code [Johnstone et al., 2021], a sophisticated state-of-the-art physical and chemical model for planetary thermospheres developed by Johnstone et al. [2018]. Johnstone et al. [2021] calculated upper atmosphere models for different N_2-CO_2-atmospheres with CO_2 mixing ratios of 99%, 75%, 50%, 25%, and 10% in the interval of 3-4 Ga ago and studied thermal escape.

For our simulations, the non-collisional part of the upper atmosphere, starting from the altitude called the exobase, is relevant, since this is where polar outflow takes place. From the upper atmosphere models calculated by Johnstone et al. [2021], we extract the altitude of the inner boundary R_{ib}, which is 2-3% below the exobase, as well as the inner boundary temperature T_{ib}. We choose to use the inner boundary instead of the actual exobase altitude since our DSMC code provides more precise results if it starts where the atmosphere is still collisional. This is because the density is higher at the inner boundary and the result is therefore less susceptible to DSMC fluctuations, which include randomness by definition. The densities of atomic nitrogen (n_{N}), oxygen (n_{O}) and carbon (n_{C}) at the inner boundary are also obtained from the profiles by Johnstone et al. [2021] and listed in Table 2.1.

CO_2	Age (Ga ago)	$R_{\rm ib}$ ($R_\oplus$)	$T_{\rm ib}$ (10^2 K)	$n_{\rm N}$ (10^{12}/m^3)	$n_{\rm O}$ (10^{12}/m^3)	$n_{\rm C}$ (10^{12}/m^3)
99%	3.0	1.02	6.22	1.15	122.51	0.76
	3.1	1.03	6.38	1.19	118.57	0.84
	3.2	1.03	7.74	1.64	118.86	0.96
	3.3	1.03	7.74	1.64	118.86	0.96
	3.4	1.03	7.34	1.27	115.44	1.04
	3.5	1.03	8.54	1.24	106.68	1.14
	3.6	1.04	10.54	1.03	81.12	1.12
	3.7	1.05	14.24	0.88	63.2	1.19
	3.8	1.08	22.74	0.62	37.92	1.16
	3.9	1.08	22.74	0.62	37.92	1.16
	4.0	1.16	44.68	0.33	15.44	0.96
75%	3.0	1.03	6.86	8.43	90.33	0.69
	3.1	1.03	7.43	8.7	87.37	0.76
	3.2	1.03	7.56	6.8	73.96	0.7
	3.3	1.03	7.56	6.8	73.96	0.7
	3.4	1.04	9.31	9.03	76.86	0.93
	3.5	1.04	11.01	8.27	62.0	0.96
	3.6	1.05	13.85	7.46	47.89	0.99
	3.7	1.07	19.23	6.89	35.56	1.09
	3.8	1.11	31.82	5.04	17.8	1.02
	3.9	1.11	31.82	5.04	17.8	1.02
	4.0	2.4	69.48	0.15	0.05	0.13
50%	3.0	1.04	8.92	13.81	58.71	0.84
	3.1	1.04	9.87	12.66	48.96	0.85
	3.2	1.04	10.19	12.84	49.98	0.9
	3.3	1.04	10.19	12.84	49.98	0.9
	3.4	1.05	13.2	13.46	42.06	1.09
	3.5	1.06	16.26	12.85	34.18	1.19
	3.6	1.08	21.48	10.95	23.22	1.2
	3.7	1.12	32.02	9.48	14.47	1.26
	3.8	1.59	84.79	1.85	1.11	0.37
	3.9	1.59	84.79	1.85	1.11	0.37
25%	3.0	1.05	12.38	20.49	31.35	1.4
	3.1	1.06	14.23	19.49	26.3	1.48
	3.2	1.06	15.08	21.23	27.11	1.65
	3.3	1.06	15.08	21.23	27.11	1.65
	3.4	1.08	20.86	17.29	16.66	1.67
	3.5	1.11	28.02	14.11	10.59	1.63
	3.6	1.21	45.6	8.71	4.53	1.3
	3.7	3.3	79.24	0.19	0.02	0.05
10%	3.0	1.07	18.49	27.36	13.36	2.63
	3.1	1.1	23.3	22.26	9.12	2.48
	3.2	1.12	27.47	17.44	6.02	2.14
	3.3	1.12	27.47	17.44	6.02	2.14
	3.4	1.35	59.03	5.67	1.14	0.92

Table 2.1: Input data of atmospheric parameters for the simulation at different ages depending on the CO_2 mixing ratio. $R_{\rm ib}$ refers to the inner boundary altitude, given in units of the Earth radius $R_\oplus = 6.371 \cdot 10^6$ m, and $T_{\rm ib}$ refers to the inner boundary temperature. We give the densities of nitrogen, oxygen, and carbon in the columns $n_{\rm N}$, $n_{\rm O}$, and $n_{\rm C}$, respectively.

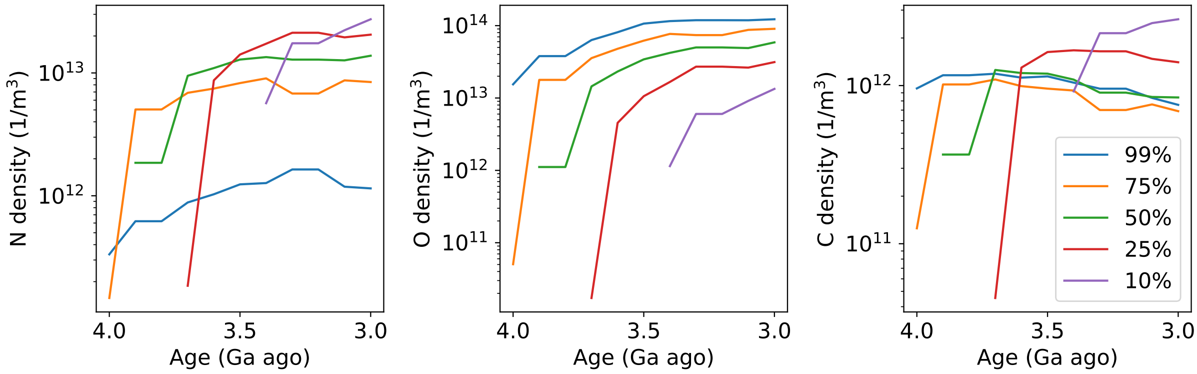

Figure 2.1: Densities of atomic nitrogen, oxygen and carbon at the inner boundary, extracted from the atmospheric profiles determined by Johnstone et al. [2021] for different CO_2 mixing ratios.

Because the X-ray flux becomes very high towards 4 Ga ago, the atmosphere becomes hydrodynamic. Johnstone et al. [2021] considered only hydrostatic cases in their simulations. Therefore, we only use CO_2 mixing ratios for which the atmosphere remains hydrostatic and for which the atmosphere is not lost due to thermal escape, based on the minimum CO_2 mixing ratio determined in Johnstone et al. [2021]. Consequently, we only use parameters from 3-3.4 Ga for 10% CO_2, 3-3.7 Ga for 25% CO_2 and 3-3.9 Ga for 50% CO_2, while for 75% and 99% CO_2 we use parameters from 3-4 Ga.

In Table 2.1, we list the parameters of the upper atmosphere for all five CO_2 mixing ratios. The densities of the three different species at the inner boundary are shown in Figure 2.1. Since our model atmosphere consists of only N_2 and CO_2, the nitrogen density is higher when the CO_2 mixing ratio is lower, and vice versa. As one would expect, a lower CO_2 mixing ratio leads to a lower oxygen density due to the oxygen being created from CO_2. However, we observe the opposite for the carbon densities, even though oxygen and carbon both originate from the dissociation of CO_2. When examining the reaction rates for the different CO_2 mixing ratios using output from the Kompot code [Johnstone et al., 2018, 2021], we find that this overabundance of atomic carbon can be explained through physical processes. Even when there is less CO_2 to start with, there are more reactions occurring that create atomic C. One of the largest differences comes from reactions that start with CO^+, which is likely due to the higher temperature that causes more CO to get ionized. As cooling through CO_2 is the main mechanism for this type of atmosphere to cool, the models with the smaller CO_2 mixing ratios end up with a greater amount of ions. This can explain the counter-intuitive overabundance of atomic C.

We show the evolution of the inner boundary altitude $R_{\rm ib}$ and temperature $T_{\rm ib}$ depending on the CO_2 mixing ratio in Figure 2.2, as determined by Johnstone et al. [2021] in their upper atmosphere models. As one would expect, a higher CO_2 mixing ratio cools the upper atmosphere and prevents its expansion, therefore leading to a lower inner boundary altitude and temperature. Due to limited data, we use the same atmospheric model for 3.2-3.3 Ga and 3.8-3.9 Ga, as can also be recognized in the plot. This is due to the fact that we use the solar XUV spectra reconstructed by Claire et al. [2012] following Johnstone et al. [2021]. However, Claire et al. [2012] only studied the Sun as the moderate rotator, while we focus on the Sun

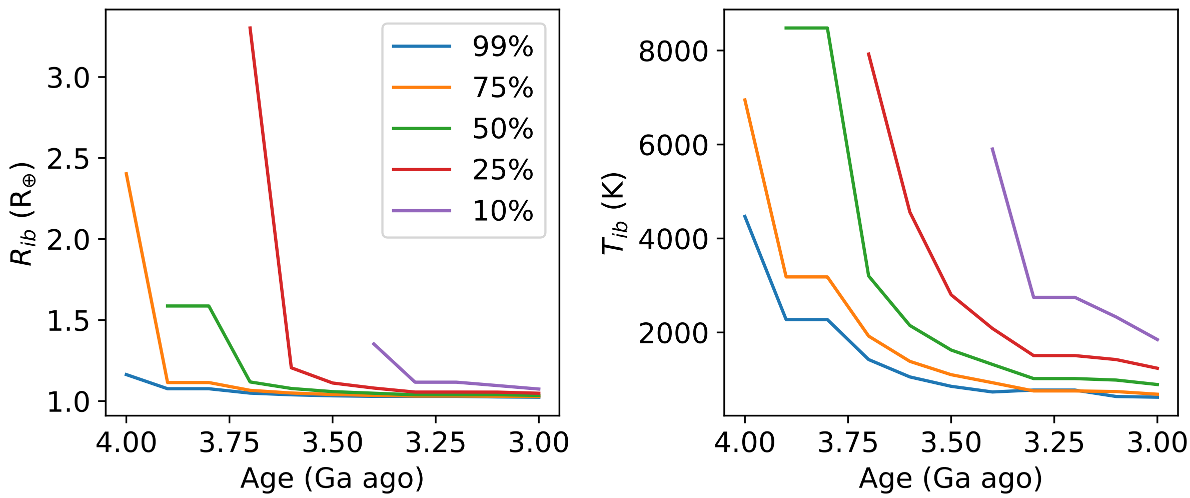

Figure 2.2: Evolution of the inner boundary over a time of 3-4 Ga depending on the CO_2 mixing ratio, as determined from the upper atmosphere models by Johnstone et al. [2021]. *Left:* Inner boundary altitude $R_{\rm ib}$. *Right:* Inner boundary temperature $T_{\rm ib}$.

as the slow rotator. This shifts the timing of the decrease of the solar activity. If the Sun evolved as a slow rotator, it had a lower initial XUV flux, but this flux also decreased slower in comparison to the moderate and fast rotator cases. This leads to the situation that we have to use the same spectra provided by Claire et al. [2012] for two different age bins of the Sun as a slow rotator.

One can further see from Table 2.1 that the number density at the inner boundary, which is inversely proportional to the mean scale height [e.g., Bauer and Lammer, 2004], depends on the XUV flux and the CO_2 mixing ratio. Both parameters influence the mean scale height at the inner boundary, which is defined as $H_{\rm ib} = k_{\rm B} T_{\rm ib}/(\bar{m}_{\rm ib} g_{\rm ib})$, where $k_{\rm B}$ is the Boltzmann-constant, and $\bar{m}_{\rm ib}$ and $g_{\rm ib}$ are the mean molecular mass and the gravitational acceleration at the inner boundary, respectively. Higher XUV fluxes and/or lower CO_2 mixing ratios will lead to the thermosphere being more expanded, which decreases $g_{\rm ib}$, but will also lead to higher dissociation rates of CO_2 and N_2. This means that the gravitational force that the planet exerts onto the particles is weaker if they are further away due to the thermosphere being more expanded, and there will be more atomic nitrogen, carbon and oxygen due to higher dissociation rates. The interplay of both, together with $T_{\rm ib}$, will increase $H_{\rm ib}$ and, consequently, reduce the respective number density at the inner boundary.

The solar radiation is also responsible for the photoionization of neutral particles. Photoionization rates for nitrogen ($\tau_{\rm i,N}$), oxygen ($\tau_{\rm i,O}$), and carbon ($\tau_{\rm i,C}$) are taken from Johnstone et al. [2021], also determined with the Kompot code. The photoionization rates of all three particle species are shown in Figure 2.3. As its name implies, this ionization process occurs through the transfer of energy from photons. There is a clear trend of higher photoionization rates going back in time, further enhancing escape rates. The rate of charge exchange, which also produces ions, is determined as $\tau_{\rm ch} = n_{\rm sw} \sigma_{\rm ch} v_{\rm sw}$, where $\sigma_{\rm ch}$ is the corresponding charge exchange cross section. We list these parameters in Table 2.2 for ages between 3-4 Ga. Those ions that are produced in the region of the open field lines are considered as escaping ions through polar outflow.

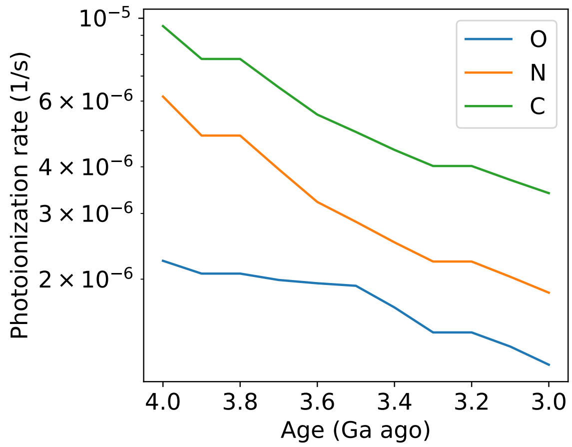

Figure 2.3: Evolution of the photoionization rates of atomic nitrogen, oxygen and carbon, as determined by Johnstone et al. [2021] using the Kompot code.

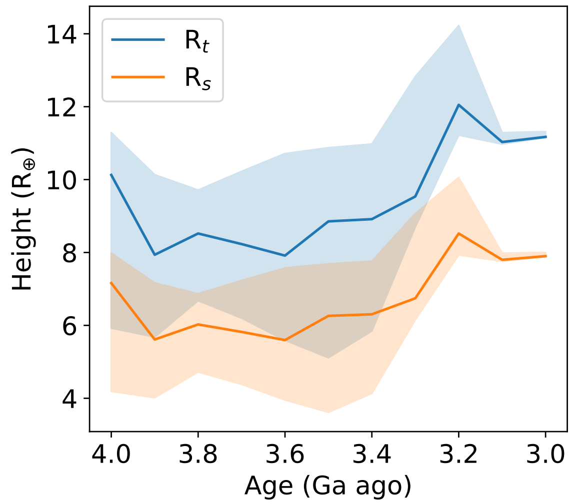

Figure 2.4: Evolution of the magnetosphere width R_t and subsolar point R_s over a time of 3-4 Ga, determined using the same version of the Paraboloid Magnetospheric Model (PMM) as in Kislyakova et al. [2020].

Age (Ga ago)	$M_e^\star/M_e$	R_s ($R_\oplus$)	R_t ($R_\oplus$)	n_{sw} ($10^6/m^3$)	v_{sw} (10^5m/s)	T_{sw} (10^5K)	$\tau_{i,N}$ (10^{-6}/s)	$\tau_{i,O}$ (10^{-6}/s)	$\tau_{i,C}$ (10^{-6}/s)	τ_{ch} (10^{-7}/s)
3.0	0.65	7.90	11.17	6.83	5.69	1.25	1.84	1.18	3.40	3.88
3.1	0.64	7.80	11.03	6.97	5.77	1.28	2.03	1.32	3.69	4.02
3.2	0.87	8.52	12.05	7.29	5.85	1.31	2.23	1.44	4.02	4.27
3.3	0.44	6.74	9.54	7.29	5.94	1.33	2.23	1.44	4.02	4.33
3.4	0.37	6.30	8.91	7.47	6.04	1.36	2.51	1.68	4.44	4.51
3.5	0.37	6.26	8.85	7.65	6.14	1.40	2.85	1.92	4.96	4.70
3.6	0.27	5.60	7.91	7.85	6.25	1.43	3.22	1.95	5.52	4.90
3.7	0.31	5.82	8.23	8.07	6.36	1.47	3.94	1.99	6.53	5.14
3.8	0.36	6.03	8.52	8.31	6.49	1.51	4.85	2.07	7.78	5.39
3.9	0.30	5.61	7.94	8.58	6.63	1.56	4.85	2.07	7.78	5.69
4.0	0.64	7.16	10.13	8.86	6.78	1.61	6.17	2.24	9.53	6.00

Table 2.2: Input parameters for the simulation that do not depend on the CO_2 mixing ratio. The parameters for the ancient dipole moment $M_e^\star/M_e$, magnetosphere subsolar point R_s and width R_t are given in units of the Earth radius $R_\oplus = 6.371 \cdot 10^6$ m. The solar wind density, velocity, and temperature are given by n_{sw}, v_{sw}, T_{sw}, respectively. The ionization rates of nitrogen, oxygen, and carbon are given by $\tau_{i,N}$, $\tau_{i,O}$, and $\tau_{i,C}$, respectively. The charge exchange rate for oxygen and nitrogen is given by τ_{ch}. The rate of charge exchange for atomic carbon is very inefficient, being in a range of only $4 - 6 \cdot 10^{-10}$/s, which is significantly lower than its photoionization rate.

To calculate the parameters of the Earth's paleomagnetosphere, we used the same adopted version of the Paraboloid Magnetospheric Model (PMM) for early Earth that we already implemented and described in detail in our preceding study [Kislyakova et al., 2020]. The PMM is a well-known dynamic model of the Earth's magnetosphere, which determines the magnetic field strength inside a paraboloid magnetopause based on the different magnetospheric large-scale

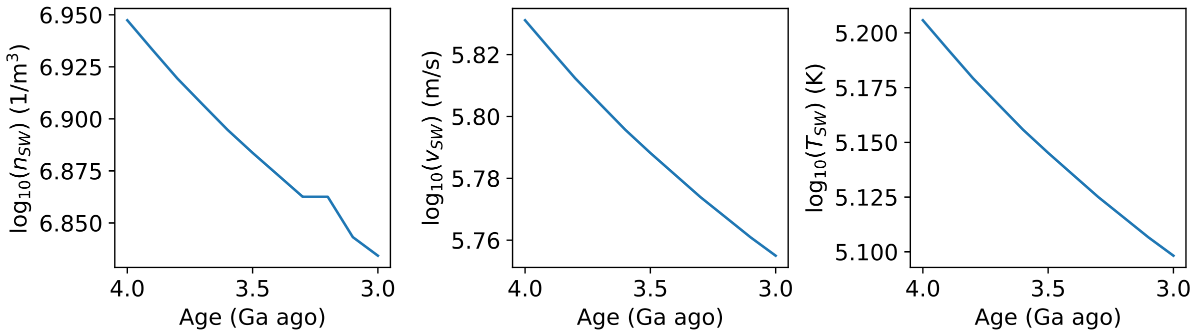

Figure 2.5: Evolution of the density (n_{sw}), velocity (v_{sw}), and temperature (T_{sw}) of the solar wind 3-4 Ga ago, calculated using the hydrodynamic wind model by Johnstone et al. [2015].

current systems [e.g., Alexeev et al., 1996, Alexeev and Feldstein, 2001]. Within the adopted PMM, Kislyakova et al. [2020] introduced the parameter $k_{\text{p}} = M_{\text{e}}^{\star}/M_{\text{e}}$, where $M_{\text{e}}^{\star}$ corresponds to the ancient magnetic dipole moment. For 3.2-4.0 Ga, we receive $M_{\text{e}}^{\star}$ by implementing the mean paleointensity values (including lower and upper limits) given in Tarduno et al. [2020], while we further take the ones suggested by Schreider et al. [2019] for 3.0 and 3.1 Ga (see Table 2.2).

The model takes the solar wind velocity v_{sw}, density n_{sw}, the z-component of the interplanetary magnetic field B_{z} and the Earth's magnetic dipole moment M_{e} as input to simulate the shape of the Earth's magnetosphere, including the radius of the subsolar point (R_{s}) and the magnetosphere width (R_{t}). The PMM calculates the subsolar point through an empirically derived formula by Shue et al. [1997, 1998] as $R_{\text{s}} = k_p^{1/3}(1.2\, p_{sw})^{-\frac{1}{6.6}}\text{R}_{\text{e}}(11.4 + AB_z)$, where $A = 0.013$ for $B_{\text{z}} \geq 0$ and $A = 0.140$ for $B_{\text{z}} < 0$, and p_{sw} is the solar wind ram pressure. The magnetosphere width can be calculated as $R_{\text{t}} = \sqrt{2R_{\text{s}}}$. Through simulating R_{s} (with R_{s} in units of the Earth radius $R_{\oplus}$), we can then further calculate the opening angle Θ of the last open field line bundle via $\Theta = \sqrt{0.52R_{\oplus}/R_{\text{s}}}$, as described in Alexeev [2006] and Kislyakova et al. [2020]. We illustrate the evolution of R_{s} and R_{t}, including lower and upper limits, in Figure 2.4. A higher compression of the magnetosphere, hence lower values of R_{s} and R_{t}, as well as a wider opening angle Θ, can enhance escape rates [e.g., Kislyakova et al., 2020].

The ancient solar wind parameters, namely the density (n_{sw}), velocity (v_{sw}), and temperature (T_{sw}), are calculated using the hydrodynamic wind model by Johnstone et al. [2015], while B_{z} is further assumed to be 0 in all our PMM simulations, since the wind model cannot not provide B_{z} and since its effect on R_{s} and R_{t} would be negligible over larger timescales. The evolution of the solar wind parameters are shown in Figure 2.5. There is a clear trend of increasing solar wind density, velocity and temperature going back in time. This translates into stronger solar winds that are more potent at enhancing atmospheric escape.

We estimate elastic collision cross sections between neutral species [Atkins and de Paula, 2000] as $\sigma_{a-b} = \pi(R_a + R_b)^2$, where σ_{a-b} is the elastic collision cross section between the two species a and b, and R_a and R_b are the atomic radii of corresponding species. Consequently, we use the following elastic collision cross sections (in m^2) in our simulations: $\sigma_{N-N} = 3.01 \cdot 10^{-19}, \sigma_{N-O} = 2.96 \cdot 10^{-19}, \sigma_{N-C} = 3.31 \cdot 10^{-19}, \sigma_{O-C} = 3.25 \cdot 10^{-19}, \sigma_{O-O} = 2.90 \cdot 10^{-19}$. The cross sections (in m^2) for charge exchange are the following: $\sigma_{N,ch} = 1 \cdot 10^{-19}, \sigma_{O,ch} = 1 \cdot 10^{-19}, \sigma_{C,ch} = 1 \cdot 10^{-22}$. Charge exchange cross sections have been taken from the ALADDIN database[1]. We list the charge exchange rates for atomic N and O in Table 2.2. At the energies of interest, charge exchange is not efficient for atomic C, which is reflected in the small cross section. The charge exchange rate of atomic C remains in a range of only $4-6\cdot10^{-10}$/s, which is significantly smaller than the photoionization rates at magnitudes of 10^{-6}/s. Therefore, the main source of carbon ions is photoionisation.

2.2 Direct Simulation Monte Carlo code

Using this input data for different ages between 3-4 Ga, we simulate the Earth's exosphere, which is the part of the atmosphere above the exobase radius where collisions are exceedingly rare [e.g., Chamberlain, 1963]. In our case, we simulate it starting from the inner boundary $R_{\rm ib}$, 2-3% below the exobase, as explained previously. We employ a DSMC kinetic model [Kislyakova et al., 2020], originally developed by Holmström et al. [2008], designed to simulate the interaction between the planet's atmosphere and the stellar or solar wind. The code considers the main processes acting on an atom in a planetary exosphere, such as ionization by the central star's radiation and wind, charge exchange between the wind protons and the atmospheric neutrals, radiation pressure, gravity, and elastic collisions between neutral particles.

Before going into the specifics of DSMC algorithms, it is important to understand the dynamical scales of gases, in particular the kinetic scale. A relevant parameter here is the Knudsen number, which expresses the degree of rarefication of a gas through $K_n = \lambda/L$. It is the ratio of the mean free path of the particles (λ) to the characteristic size of the system (L). The mean free path represents an average length that a particle can travel before colliding with another particle. Figure 2.6 shows three different physical scales with which one can describe the dynamics of dilute gases. On the left one can see the smallest scale, namely the quantum scale. At such small scales, intermolecular interactions dominate. On the right, one can see a gas that can be described by continuum hydrodynamic fields. In between these two is the kinetic scale, at which the discrete molecular nature of the gas dominates the system dynamics. The kinetic scale exhibits a relatively high Knudsen number, since the mean free path of a particle is relatively large compared to the system size. Our particle code is a kinetic model, which means that it simulates a gas on the kinetic scale. This means that the gas is quite rarefied and the particles do not collide very frequently. At this scale, the collisions between the gas molecules can be modeled using as stochastic events with specified rates [Garcia, 2011].

Developed by Bird [1976], DSMC algorithms were designed to simulate gases at the kinetic scale. This method is able to accurately model flows with high Knudsen numbers and is one of the most common numerical methods used for the molecular simulation of dilute gases. The computational volume is filled with particles that are assigned a random velocity drawn from a specified distribution. As is typical for Monte Carlo simulations, DSMC also relies on repeated random sampling to obtain numerical results. In this method, a variety of probability distributions are used for different purposes, from which the random numbers are drawn. Direct simulation in this case means that the particles are being simulated directly. DSMC can be

[1] https://www-amdis.iaea.org/ALADDIN/

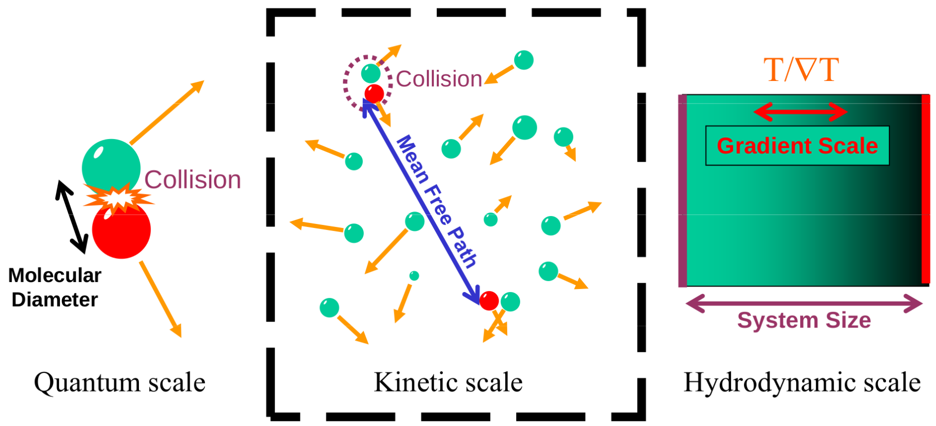

Figure 2.6: Different scales for dynamics of dilute gases [Garcia, 2011]. DSMC algorithms simulate gases at the kinetic scale.

considered an application of of Monte Carlo methods to gas dynamics to model rarefied gas flows.

In the case of our particle code, neutral oxygen, nitrogen, and carbon particles are launched every second at a random location at the spherical inner boundary. Their randomly assigned velocity depends on the atmosphere's temperature and is drawn from a Maxwellian distribution as described in Kislyakova et al. [2014]. Particles are then followed in the 3-D simulation domain considering all the interactions with the solar wind. Charge exchange only happens in the area of the open field lines, that is, beyond the magnetopause or in the polar areas restricted by the opening angle Θ. Neutral particles can be photoionized by the solar radiation everywhere where they are exposed to sunlight, but are only accounted for as escaping ions if they have been produced in the polar regions. The code does not follow the ions along open field lines, but simply counts how many ions of each species are being produced.

How many ions actually escape from the polar region is not completely clear. Where the ions end up mostly depends on their initial velocity and location. While some ions end up in different regions of the Earth's magnetosphere, a part of them may even be recycled from way back in the magnetosphere and return to the Earth. However, at least for oxygen ions, Ebihara et al. [2006] showed that most of them do end up lost from the atmosphere. To keep it simple, we consider all produced ions to be escaping through polar outflow and use this as an upper limit for escape. Satellite observations do in fact support a low return rate of ionospheric ions, meaning that a significant amount of escaping ions are truly lost to interplanetary space [Newell et al., 2010].

We use a new version of the code from Kislyakova et al. [2020] that includes identical processes but does not use `FLASH4` [Fryxell et al., 2000]. `FLASH4` is a fully parallelized code that was used in the DSMC model to provide adaptive grids and parallelisation. The version of the DSMC code we use in the current article does not rely on `FLASH4` for these things. The current version utilises a Cartesian grid and can be run on a local machine with the same amount of metaparticles as the old code version with `FLASH4` on a server.

Using this method, we estimate the ionization rates per second of nitrogen, oxygen and carbon atoms, which we assume as a proxy for the polar outflow escape rate. It is reasonable to assume that only ionized particles can escape along the open field lines, since they can be accelerated by the electric fields along the open field lines, which lead away from the planet. Depending on their energy, these ions can end up in different regions of the Earth's magnetosphere, such as the magnetopause, the distant tail, and the ring currents, or fall back down to the atmosphere [Seki et al., 2001, Ebihara et al., 2006]. We use the ionization rates obtained from the simulations as upper limits of escape through polar outflow assuming all ionized particles do escape.

Chapter 3

Evolution of Earth's Oxygen, Nitrogen, and Carbon Polar Outflow in the Archean Eon

Using the previously described methods and input parameters, I simulated the Earth's exosphere to determine the ion production rates of nitrogen, oxygen and carbon for the Archean Earth, which are used as a proxy for the polar outflow escape rate. With this work, we find that lower CO_2 mixing ratios significantly increase atmospheric escape via polar outflow. Our results indicate that the CO_2 mixing ratio in the early Archean may have been over 25%, possibly even 50%, in order to avoid excessive atmospheric loss through polar outflow. This is in agreement with other studies that suggest a high CO_2 mixing ratio during the early Archean [e.g., Johnstone et al., 2021] along with only modest atmospheric escape of nitrogen [e.g., Cartigny and Marty, 2013].

This research work for my thesis was made into an article and submitted to the journal Earth and Planetary Science Letters (EPSL). The next few pages show my originally submitted manuscript, where one can find more details about the results and discussion.

Publication details

Title: Evolution of Earth's Oxygen, Nitrogen, and Carbon Polar Outflow in the Archean Eon
Authors: Natalie Grasser; Kristina Kislyakova; Manuel Scherf; Helmut Lammer; Gwenaël van Looveren
Journal: Earth and Planetary Science Letters
Submitted: April 13, 2023
Status: Under review
Own contributions: I performed all of the numerical simulations, did the bulk of the data analysis and wrote most of the article's text.

Evolution of Earth's Oxygen, Nitrogen, and Carbon Polar Outflow in the Archean Eon

Natalie Grasser[a,*], Kristina Kislyakova[a], Manuel Scherf[b], Helmut Lammer[b], Gwenaël van Looveren[a]

[a]*University of Vienna, Department of Astrophysics, Türkenschanzstrasse 17, Vienna, 1180, Austria*
[b]*Space Research Institute, Austrian Academy of Sciences, Schmiedlstrasse 6, Graz, 8042, Austria*

Abstract

The habitability of Earth significantly depends on the evolution of its atmospheric properties, which are strongly influenced by escape processes. Polar outflow, which encompasses the atmospheric escape of ions through the open field lines of the Earth's magnetosphere, is the dominant escape process for modern Earth and likely played a significant role in Earth's early history as well. In this article, we investigate the evolution of Earth's polar outflow during the Archean eon 3-4 gigayears (Ga) ago for an N_2-CO_2 atmosphere. For this, we use a kinetic direct simulation Monte Carlo (DSMC) particle code to simulate the interactions between the solar wind and the Earth's upper atmosphere. We explore the effects of different CO_2 mixing ratios (10%,25%,50%,75%,99%) on the polar outflow escape rates of oxygen, nitrogen and carbon. Using the ion production rates as a proxy for polar outflow, our results indicate that during the time 3.6-4.0 Ga ago, a CO_2 mixing ratio larger than 25% may have been necessary to avoid excessive escape via polar outflow. Close to 4 Ga ago, even 50% CO_2 may have been necessary due to the stronger solar winds. Our results align with other studies also suggesting a similarly high CO_2 mixing ratio in the early Archean.

Keywords: Earth, Archean, polar outflow, atmospheric escape, direct simulation Monte Carlo, carbon dioxide

1. Introduction

The habitability of a planet does not only depend on its distance to its host star, but also on the presence and maintenance of an atmosphere providing sufficiently high temperature and pressure to maintain liquid water on a planet's surface (e.g., Huang, 1959; Kasting et al., 1993; Kopparapu et al., 2013). The evolution of a planet's atmosphere is to a large extent governed by its escape to space, and many factors play a role including the physical characteristics of a planet, dynamics of its orbit and rotation, and outgassing history (Van Hoolst et al., 2019). The evolution of the short-wavelength solar radiation and wind, as well as the evolution of the atmosphere's composition, are factors that strongly affect the extent of atmospheric escape (e.g., Chamberlain 1963; Chamberlain and Hunten 1987; Gronoff et al. 2020).

Atmospheric escape can be divided into thermal and non-thermal processes. Thermal escape processes arise from the heating and hence accelerating of the upper atmosphere particles and are heavily influenced by the host star's X-ray and extreme ultraviolet radiation (together XUV; wavelength range 1–400 nm, as in Johnstone et al., 2018, 2021). In contrast, non-thermal escape processes encompass various other complex interactions between the stellar wind and atmospheric particles, such as photochemical escape, stellar wind charge exchange, ion pickup and polar outflow (e.g., Lammer 2013; Gronoff et al. 2020). The Sun's XUV flux and wind have evolved dramatically and were significantly higher in Earth's early history (e.g., Güdel, 2007; Johnstone et al., 2015; Tu et al., 2015), which enhanced atmospheric escape from the planet (e.g., Lichtenegger et al., 2010; Johnstone et al., 2021).

According to Tian et al. (2008a,b), modern Earth's N_2-O_2-dominated atmosphere would rapidly escape thermally if exposed to solar radiation as strong as it was during the early Archean eon (4-2.4 Ga), while a recent model by Nakayama et al. (2022) yields contrasting results on the thermospheric structure. The atmospheric composition prior to the Great Oxygenation Event (GOE) was significantly different than at present-day with no appreciable O_2 (e.g., Lyons et al., 2014;

*Corresponding author at: University of Vienna, Department of Astrophysics, Türkenschanzstrasse 17, 1180 Vienna, Austria.
E-mail address: natalie.grasser@univie.ac.at (N. Grasser).

Stüeken et al., 2020). According to geochemical measurements, the CO_2 partial pressure may additionally have been significantly higher than in the current atmosphere (e.g., Kanzaki and Murakami 2015). Since CO_2 acts as a coolant in the upper atmosphere, a higher mixing ratio of this gas leads to lower atmospheric thermal (e.g., Johnstone et al., 2021) and non-thermal escape rates (e.g., Lichtenegger et al., 2010), but this process has not been studied quantitatively for polar outflow. An atmosphere stable against atmospheric erosion is in agreement with significant geological evidence on the presence of liquid water and life during the Archean eon (Javaux 2019).

Johnstone et al. (2021) have further shown that a nitrogen-dominated atmosphere (at least without appreciable amounts of O_2) prior to the GOE should have had a CO_2 mixing ratio of at least 40% at the start of the Archean to prevent rapid escape of the atmosphere due to the young Sun's XUV radiation; such CO_2 mixing ratio would also be high enough to resolve the Faint Young Sun Paradox (e.g., Feulner, 2012; Charnay et al., 2020). However, this study did not take into account non-thermal escape processes.

Some non-thermal ion loss processes, including polar outflow, are governed by a planet's intrinsic magnetic field. Polar outflow, also referred to as polar wind, ion outflow or ionospheric outflow, occurs when charged atmospheric particles escape along the field lines of a planet's magnetosphere (e.g., Gronoff et al., 2020). A planetary magnetosphere can, on one hand, protect an atmosphere from stellar wind erosion; on the other hand, ions can escape from the open field line bundles if sufficient energy and momentum exchange occurs between the solar wind and atmospheric particles (e.g., Blackman and Tarduno, 2018). On present-day Earth, atmospheric escape is indeed dominated by polar outflow from the open field line bundle (e.g., Gunell et al., 2018) and it has likely been the dominant escape process back until at least the GOE (Kislyakova et al., 2020). Whether polar outflow was dominating atmospheric losses during the Archean eon is yet unknown. However, it is known that Earth's magnetic field has existed as early as 4.2 Ga, even though its field strength was likely weaker during the Archean eon (Tarduno et al. 2015, 2020).

In this follow-up study to our previous work (Kislyakova et al., 2020), we investigate the evolution of the polar ion outflow rates from early Earth (3-4 Ga) for N_2-CO_2-atmospheres with different CO_2 mixing ratios (99%, 75%, 50%, 25%, 10%) considering the evolving solar wind, Earth's paleomagnetosphere and atmospheric composition. We assume that the young Sun evolved as a slow rotator (Tu et al., 2015), because otherwise Earth's atmosphere would have likely been lost due to thermal escape (Johnstone et al., 2021). For this purpose, we employ the same kinetic Direct Simulation Monte Carlo (DSMC) particle model as in Kislyakova et al. (2020) through which the effects of different CO_2 mixing ratios on atmosphere maintenance can be explored. We describe our methods and input parameters in Section 2, present and discuss our results in Section 3 and conclude our work in Section 4.

2. Methods and input parameters

2.1. Input data

As input data for the simulation, we adopt the upper atmosphere densities, temperatures and ionization rates determined for early Earth with the Kompot Code (Johnstone et al., 2021), a sophisticated state-of-the-art physical and chemical model for planetary thermospheres developed by Johnstone et al. (2018). Johnstone et al. (2021) calculated upper atmosphere models for different N_2-CO_2-atmospheres with CO_2 mixing ratios of 99%, 75%, 50%, 25%, and 10% in the interval of 3-4 Ga and studied thermal escape.

For our simulations, the non-collisional part of the upper atmosphere, starting from the altitude called the exobase, is relevant, since this is where polar outflow takes place. From the upper atmosphere models calculated by Johnstone et al. (2021), we extract the altitude of the inner boundary R_{ib}, which is 2-3% below the exobase, as well as the inner boundary temperature T_{ib}. We choose to use the inner boundary instead of the actual exobase altitude since our DSMC code provides more precise results if it starts where the atmosphere is still collisional. This is because the density is higher at the inner boundary and the result is therefore less susceptible to DSMC fluctuations, which include randomness by definition. The densities of atomic nitrogen (n_N), oxygen (n_O) and carbon (n_C) at the inner boundary are also obtained from the profiles by Johnstone et al. (2021) and listed in Table 1.

Because the X-ray flux becomes very high towards 4 Ga ago, the atmosphere becomes hydrodynamic. Johnstone et al. (2021) considered only hydrostatic cases in their simulations. Therefore, we only use CO_2 mixing ratios for which the atmosphere remains hydrostatic and for which the atmosphere is not lost due to thermal escape, based on the minimum CO_2 mixing ratio determined in Johnstone et al. (2021). Consequently, we only use parameters from 3-3.4 Ga for 10% CO_2, 3-3.7 Ga for 25% CO_2 and 3-3.9 Ga for 50% CO_2, while for 75% and 99% CO_2 we use parameters from 3-4 Ga.

In Table 1, we list the parameters of the upper atmosphere for all five CO_2 mixing ratios. Since our model atmosphere consists of only N_2 and CO_2, the nitrogen density is higher when the CO_2 mixing ratio is lower, and vice versa. As one would expect, a lower CO_2 mixing ratio leads to a lower oxygen density due to the oxygen being created from CO_2. However, we observe the opposite for the carbon densities, even though oxygen and carbon both originate from the dissociation of CO_2. When examining the reaction rates for the different CO_2 mixing ratios using output from the Kompot code (Johnstone et al., 2018, 2021), we find that this overabundance of atomic carbon can be explained through physical processes. Even when there is less CO_2 to start with, there are more reactions occurring that create atomic C. One of the largest differences comes from reactions that start with CO^+, which is likely due to the higher temperature that causes more CO to get ionized. As cooling through CO_2 is the main mechanism for this type of atmosphere to cool, the models with the smaller CO_2 mixing ratios end up with a greater amount of ions. This can explain the counter-intuitive overabundance of atomic C.

We show the evolution of the inner boundary altitude R_{ib} and temperature T_{ib} depending on the CO_2 mixing ratio in Figure 1, as determined by Johnstone et al. (2021) in their upper atmosphere models. As one would expect, a higher CO_2 mixing ratio cools the upper atmosphere and prevents its expansion, therefore leading to a lower inner boundary altitude and temperature. Due to limited data, we use the same atmospheric model for 3.2-3.3 Ga and 3.8-3.9 Ga, as can also be recognized in the plot. This is due to the fact that we use the solar XUV spectra reconstructed by Claire et al. (2012) following Johnstone et al. (2021). However, Claire et al. (2012) only studied the Sun as the moderate rotator, while we focus on the Sun as the slow rotator. This shifts the timing of the decrease of the solar activity. If the Sun evolved as a slow rotator, it had a lower initial XUV flux, but this flux also decreased slower in comparison to the moderate and fast rotator cases. This leads to the situation that we have to use the same spectra provided by Claire et al. (2012) for two different age bins of the Sun as a slow rotator.

One can further see from Table 1 that the number density at the inner boundary, which is inversely proportional to the mean scale height (e.g., Bauer and Lammer, 2004), depends on the XUV flux and the CO_2 mixing ratio. Both parameters influence the mean scale height at the inner boundary which is defined as $H_{\mathrm{ib}} = k_{\mathrm{B}} T_{\mathrm{ib}} / (\bar{m}_{\mathrm{ib}} g_{\mathrm{ib}})$, where k_{B} is the Boltzmann-constant, and $\bar{m}_{\mathrm{ib}}$ and g_{ib} are the mean molecular mass and the gravitational acceleration at the inner boundary, respectively. Higher XUV fluxes and/or lower CO_2 mixing ratios will lead to the thermosphere being more expanded, which decreases g_{ib}, but will also lead to higher dissociation rates of CO_2 and N_2; the interplay of both, together with T_{ib}, will increase H_{ib} and, consequently, reduce the respective number density at the inner boundary.

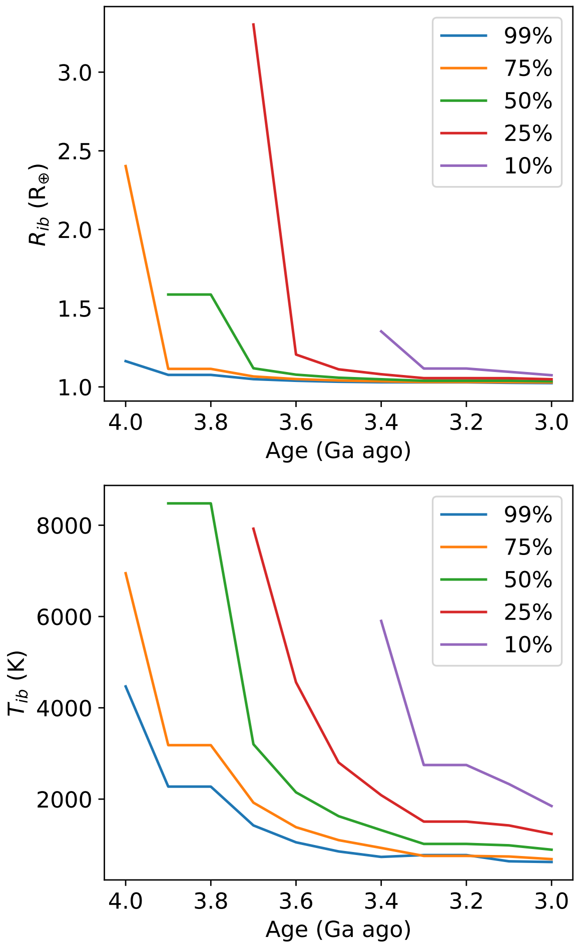

Figure 1: Evolution of the inner boundary over a time of 3-4 Ga depending on the CO_2 mixing ratio, as determined from the upper atmosphere models by Johnstone et al. (2021). *Top:* Inner boundary altitude R_{ib}. *Bottom:* Inner boundary temperature T_{ib}.

To calculate the parameters of the Earth's paleomagnetosphere, we used the same adopted version of the Paraboloid Magnetospheric Model (PMM) for early Earth that we already implemented and described in detail in our preceding study (Kislyakova et al., 2020). The PMM is a well-known dynamic model of the Earth's magnetosphere, which determines the magnetic field strength inside a paraboloid magnetopause based on the different magnetospheric large-scale current sys-

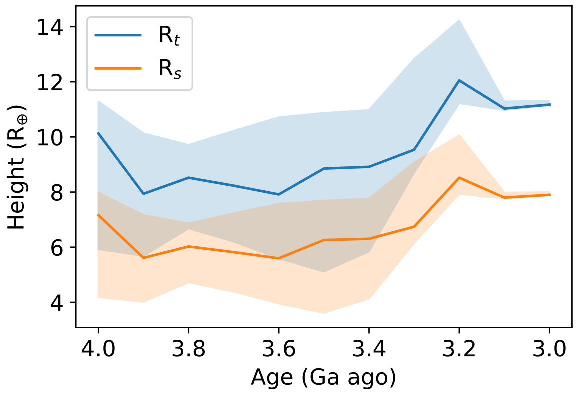

Figure 2: Evolution of the magnetosphere width R_t and subsolar point R_s over a time of 3-4 Ga, determined using the same version of the Paraboloid Magnetospheric Model (PMM) as in Kislyakova et al. (2020).

tems (e.g., Alexeev et al., 1996; Alexeev and Feldstein, 2001). Within the adopted PMM, Kislyakova et al. (2020) introduced the parameter $k_p = M_e^\star / M_e$, where $M_e^\star$ corresponds to the ancient magnetic dipole moment. For 3.2-4.0 Ga, we receive $M_e^\star$ by implementing the mean paleointensity values (including lower and upper limits) given in Tarduno et al. (2020), while we further take the ones suggested by Schreider et al. (2019) for 3.0 and 3.1 Ga (see Table 2).

The model takes the solar wind velocity v_{sw}, density n_{sw}, the z-component of the interplanetary magnetic field B_z and the Earth's magnetic dipole moment M_e as input to simulate the shape of the Earth's magnetosphere, including the radius of the subsolar point (R_s) and the magnetosphere width (R_t). The PMM calculates the subsolar point through an empirically derived formula by Shue et al. (1997, 1998) as $R_s = k_p^{1/3}(1.2\,p_{sw})^{-\frac{1}{6.6}} \mathrm{R_e}(11.4 + AB_z)$, where $A = 0.013$ for $B_z \geq 0$ and $A = 0.140$ for $B_z < 0$, and p_{sw} is the solar wind ram pressure. The magnetosphere width can be calculated as $R_t = \sqrt{2}R_s$. Through simulating R_s (with R_s in units of the Earth radius $R_\oplus$), we can then further calculate the opening angle Θ of the last open field line bundle via $\Theta = \sqrt{0.52 R_\oplus / R_s}$, as described in Alexeev (2006) and Kislyakova et al. (2020). We illustrate the evolution of R_s and R_t, including lower and upper limits, in Figure 2. A higher compression of the magnetosphere, hence lower values of R_s and R_t, as well as a wider opening angle Θ, can enhance escape rates (e.g., Kislyakova et al., 2020).

The ancient solar wind parameters, namely the density (n_{sw}), velocity (v_{sw}), and temperature (T_{sw}), are calculated using the hydrodynamic wind model by Johnstone et al. (2015), while B_z is further assumed to be 0 in all our PMM simulations, since the wind model cannot not provide B_z and since its effect on R_s and R_t would be negligible over larger timescales. Photoionization rates for nitrogen ($\tau_{i,N}$), oxygen ($\tau_{i,O}$), and carbon ($\tau_{i,C}$) are taken from Johnstone et al. (2021), also determined with the Kompot code. The rate of charge exchange, which also produces ions, is determined as $\tau_{ch} = n_{sw}\sigma_{ch}v_{sw}$, where σ_{ch} is the corresponding charge exchange cross section. We list these parameters in Table 2 for ages between 3-4 Ga.

We estimate elastic collision cross sections between neutral species (Atkins and de Paula, 2000) as $\sigma_{a-b} = \pi(R_a + R_b)^2$, where σ_{a-b} is the elastic collision cross section between the two species a and b, and R_a and R_b are the atomic radii of corresponding species. Consequently, we use the following elastic collision cross sections (in m^2) in our simulations: $\sigma_{N-N} = 3.01 \cdot 10^{-19}, \sigma_{N-O} = 2.96 \cdot 10^{-19}, \sigma_{N-C} = 3.31 \cdot 10^{-19}, \sigma_{O-C} = 3.25 \cdot 10^{-19}, \sigma_{O-O} = 2.90 \cdot 10^{-19}$. The cross sections (in m^2) for charge exchange are the following: $\sigma_{N,ch} = 1 \cdot 10^{-19}, \sigma_{O,ch} = 1 \cdot 10^{-19}, \sigma_{C,ch} = 1 \cdot 10^{-22}$. Charge exchange cross sections have been taken from the ALADDIN database[1]. We list the charge exchange rates for atomic N and O in Table 2. At the energies of interest, charge exchange is not efficient for atomic C, which is reflected in the small cross section. The charge exchange rate of atomic C remains in a range of only $4 - 6 \cdot 10^{-10}$/s, which is significantly smaller than the photoionization rates at magnitudes of 10^{-6}/s. Therefore, the main source of carbon ions is photoionisation.

2.2. *Direct Simulation Monte Carlo code*

Using this input data for different ages between 3-4 Ga, we simulate the Earth's exosphere, which is the part of the atmosphere above the exobase radius where collisions are exceedingly rare (e.g., Chamberlain, 1963). In our case, we simulate it starting from the inner boundary R_{ib}, 2-3% below the exobase, as explained previously. We employ a DSMC kinetic model (Kislyakova et al., 2020), originally developed by Holmström et al. (2008), designed to simulate the interaction between the planet's atmosphere and the stellar or solar wind. The code considers the main processes acting on an atom in a planetary exosphere, such as ionization by the central star's radiation and wind, charge exchange between the wind protons and the atmospheric neutrals, radiation pressure, gravity, and elastic collisions between neutral particles.

[1] https://www-amdis.iaea.org/ALADDIN/

CO_2	Age (Ga ago)	R_{ib} ($R_\oplus$)	T_{ib} (10^2 K)	n_N ($10^{12}/m^3$)	n_O ($10^{12}/m^3$)	n_C ($10^{12}/m^3$)
99%	3.0	1.02	6.22	1.15	122.51	0.76
	3.1	1.03	6.38	1.19	118.57	0.84
	3.2	1.03	7.74	1.64	118.86	0.96
	3.3	1.03	7.74	1.64	118.86	0.96
	3.4	1.03	7.34	1.27	115.44	1.04
	3.5	1.03	8.54	1.24	106.68	1.14
	3.6	1.04	10.54	1.03	81.12	1.12
	3.7	1.05	14.24	0.88	63.2	1.19
	3.8	1.08	22.74	0.62	37.92	1.16
	3.9	1.08	22.74	0.62	37.92	1.16
	4.0	1.16	44.68	0.33	15.44	0.96
75%	3.0	1.03	6.86	8.43	90.33	0.69
	3.1	1.03	7.43	8.7	87.37	0.76
	3.2	1.03	7.56	6.8	73.96	0.7
	3.3	1.03	7.56	6.8	73.96	0.7
	3.4	1.04	9.31	9.03	76.86	0.93
	3.5	1.04	11.01	8.27	62.0	0.96
	3.6	1.05	13.85	7.46	47.89	0.99
	3.7	1.07	19.23	6.89	35.56	1.09
	3.8	1.11	31.82	5.04	17.8	1.02
	3.9	1.11	31.82	5.04	17.8	1.02
	4.0	2.4	69.48	0.15	0.05	0.13
50%	3.0	1.04	8.92	13.81	58.71	0.84
	3.1	1.04	9.87	12.66	48.96	0.85
	3.2	1.04	10.19	12.84	49.98	0.9
	3.3	1.04	10.19	12.84	49.98	0.9
	3.4	1.05	13.2	13.46	42.06	1.09
	3.5	1.06	16.26	12.85	34.18	1.19
	3.6	1.08	21.48	10.95	23.22	1.2
	3.7	1.12	32.02	9.48	14.47	1.26
	3.8	1.59	84.79	1.85	1.11	0.37
	3.9	1.59	84.79	1.85	1.11	0.37
25%	3.0	1.05	12.38	20.49	31.35	1.4
	3.1	1.06	14.23	19.49	26.3	1.48
	3.2	1.06	15.08	21.23	27.11	1.65
	3.3	1.06	15.08	21.23	27.11	1.65
	3.4	1.08	20.86	17.29	16.66	1.67
	3.5	1.11	28.02	14.11	10.59	1.63
	3.6	1.21	45.6	8.71	4.53	1.3
	3.7	3.3	79.24	0.19	0.02	0.05
10%	3.0	1.07	18.49	27.36	13.36	2.63
	3.1	1.1	23.3	22.26	9.12	2.48
	3.2	1.12	27.47	17.44	6.02	2.14
	3.3	1.12	27.47	17.44	6.02	2.14
	3.4	1.35	59.03	5.67	1.14	0.92

Table 1: Input data of atmospheric parameters for the simulation at different ages depending on the CO_2 mixing ratio. R_{ib} refers to the inner boundary altitude, given in units of the Earth radius $R_\oplus = 6.371 \cdot 10^6$ m, and T_{ib} refers to the inner boundary temperature. We give the densities of nitrogen, oxygen, and carbon in the columns n_N, n_O, and n_C, respectively.

Age (Ga ago)	$M_e^\star/M_e$	R_s ($R_\oplus$)	R_t ($R_\oplus$)	n_{sw} (10^6/m^3)	v_{sw} (10^5m/s)	T_{sw} (10^5K)	$\tau_{i,N}$ (10^{-6}/s)	$\tau_{i,O}$ (10^{-6}/s)	$\tau_{i,C}$ (10^{-6}/s)	τ_{ch} (10^{-7}/s)
3.0	0.65	7.90	11.17	6.83	5.69	1.25	1.84	1.18	3.40	3.88
3.1	0.64	7.80	11.03	6.97	5.77	1.28	2.03	1.32	3.69	4.02
3.2	0.87	8.52	12.05	7.29	5.85	1.31	2.23	1.44	4.02	4.27
3.3	0.44	6.74	9.54	7.29	5.94	1.33	2.23	1.44	4.02	4.33
3.4	0.37	6.30	8.91	7.47	6.04	1.36	2.51	1.68	4.44	4.51
3.5	0.37	6.26	8.85	7.65	6.14	1.40	2.85	1.92	4.96	4.70
3.6	0.27	5.60	7.91	7.85	6.25	1.43	3.22	1.95	5.52	4.90
3.7	0.31	5.82	8.23	8.07	6.36	1.47	3.94	1.99	6.53	5.14
3.8	0.36	6.03	8.52	8.31	6.49	1.51	4.85	2.07	7.78	5.39
3.9	0.30	5.61	7.94	8.58	6.63	1.56	4.85	2.07	7.78	5.69
4.0	0.64	7.16	10.13	8.86	6.78	1.61	6.17	2.24	9.53	6.00

Table 2: Input parameters for the simulation that do not depend on the CO_2 mixing ratio. The parameters for the ancient dipole moment $M_e^\star/M_e$, magnetosphere subsolar point R_s and width R_t are given in units of the Earth radius $R_\oplus = 6.371 \cdot 10^6$ m. The solar wind density, velocity, and temperature are given by n_{sw}, v_{sw}, T_{sw}, respectively. The ionization rates of nitrogen, oxygen, and carbon are given by $\tau_{i,N}$, $\tau_{i,O}$, and $\tau_{i,C}$, respectively. The charge exchange rate for oxygen and nitrogen is given by τ_{ch}. The rate of charge exchange for atomic carbon is very inefficient, being in a range of only $4-6 \cdot 10^{-10}$/s, which is significantly lower than its photoionization rate.

Every second, the code launches neutral oxygen, nitrogen, and carbon particles at a random location at the spherical inner boundary. Their randomly assigned velocity depends on the atmosphere's temperature and is drawn from a Maxwellian distribution as described in Kislyakova et al. (2014). Particles are then followed in the 3-D simulation domain considering all the interactions with the solar wind. Charge exchange only happens in the area of the open field lines, that is, beyond the magnetopause or in the polar areas restricted by the opening angle Θ (see the first panel in Figure 3). Neutral particles can be photoionized everywhere where they are exposed to sunlight, but are only accounted for as escaping ions if they have been produced in the polar regions. The code does not follow the ions along open field lines.

How many ions actually escape from the polar region is not completely clear. Where the ions end up mostly depends on their initial velocity and location. While some ions end up in different regions of the Earth's magnetosphere, a part of them may even be recycled from way back in the magnetosphere and return to the Earth. However, at least for oxygen ions, Ebihara et al. (2006) showed that most of them do end up lost from the atmosphere. To keep it simple, we consider all produced ions to be escaping through polar outflow and use this as an upper limit for escape. Satellite observations do in fact support a low return rate of ionospheric ions, meaning that a significant amount of escaping ions are truly lost to interplanetary space (Newell et al., 2010).

We use a new version of the code from Kislyakova et al. (2020) that includes identical processes but does not use `FLASH4` (Fryxell et al., 2000). `FLASH4` is a fully parallelized code that was used in the DSMC model to provide adaptive grids and parallelisation. The version of the DSMC code we use in the current article does not rely on `FLASH4` for these things. The current version utilises a Cartesian grid and can be run on a local machine with the same amount of metaparticles as the old code version with `FLASH4` on a server.

Using this method, we estimate the ionization rates per second of nitrogen, oxygen and carbon atoms, which we assume as a proxy for the polar outflow escape rate. It is reasonable to assume that only ionized particles can escape along the open field lines, since they can be accelerated by the electric fields along the open field lines, which lead away from the planet. Depending on their energy, these ions can end up in different regions of the Earth's magnetosphere, such as the magnetopause, the distant tail, and the ring currents, or fall back down to the atmosphere (Seki et al., 2001; Ebihara et al., 2006). We use the ionization rates obtained from the simulations as upper limits of escape through polar outflow assuming all ionized particles do escape.

3. Results and discussion

Using the model results described in Sect. 2, we assume CO_2/N_2 mixing ratios of 99%, 75%, 50%, 25%, and 10% for the main atmosphere on early Earth during the Archean epoch. Table 1 shows the densities and temperatures of atomic species close to the exobase, which are products of the photodissociation of the molecules. These values are then used as an input

CO_2	Age (Ga ago)	$\tau_{esc,N+}$ (10^{24}/s)	$\tau_{esc,O+}$ (10^{24}/s)	$\tau_{esc,C+}$ (10^{24}/s)
99%	3.0	2.97	201.39	2.46
	3.1	2.23	185.72	4.76
	3.2	4.14	336.07	4.71
	3.3	5.92	241.97	8.09
	3.4	5.97	421.04	7.19
	3.5	7.72	471.34	15.57
	3.6	11.89	499.71	27.3
	3.7	17.11	509.84	68.73
	3.8	66.16	619.91	301.06
	3.9	73.65	659.64	342.07
	4.0	620.71	596.56	3800.94
75%	3.0	23.98	115.85	10.88
	3.1	23.7	165.19	16.49
	3.2	32.64	125.04	15.71
	3.3	26.12	200.07	16.32
	3.4	52.75	419.83	61.45
	3.5	55.67	383.45	117.91
	3.6	93.36	464.69	345.67
	3.7	152.6	394.79	1231.43
	3.8	289.84	401.75	4984.54
	3.9	348.38	449.02	5240.04
	4.0	5394.44	896.18	8098.43
50%	3.0	57.87	132.53	35.09
	3.1	63.92	138.34	47.56
	3.2	52.27	105.44	53.95
	3.3	82.91	184.52	70.74
	3.4	113.6	301.21	244.44
	3.5	150.71	299.82	575.49
	3.6	274.9	323.29	1542.8
	3.7	458.22	360.91	5165.15
	3.8	6944.54	3349.38	22651.98
	3.9	7502.11	3723.15	23770.07
25%	3.0	129.11	134.41	97.07
	3.1	129.91	122.99	174.28
	3.2	167.68	130.58	238.84
	3.3	182.26	156.69	302.06
	3.4	310.54	142.03	925.82
	3.5	351.45	186.86	2283.73
	3.6	700.7	311.81	8520.47
	3.7	48705.45	2736.05	26471.78
10%	3.0	204.64	59.06	292.12
	3.1	194.49	60.8	582.19
	3.2	230.63	74.5	814.33
	3.3	284.89	75.96	1008.31
	3.4	664.34	1749.94	8638.89

Table 3: Escape rates of ionized nitrogen ($\tau_{esc,N+}$), oxygen ($\tau_{esc,O+}$), and carbon ($\tau_{esc,C+}$) depending on the CO_2 mixing ratio and age.

for the DSMC model. Figure 3 shows example slices of the particle clouds of neutral and ionized nitrogen, oxygen and carbon for various scenarios in for a qualitative comparison. Due to the greater amount of carbon meta-particles, only every 5th one is plotted. Since C atoms are a bit lighter and more abundant than O and N atoms, C particles appear more dispersed.

In the first and second panel, the particle clouds for a CO_2 mixing ratio of 99% and 25% at an age of 3.6 Ga ago are shown. One can clearly see that for lower CO_2 mixing ratios, the atmosphere is significantly more ionized and expanded due to the reduced IR-cooling of the upper atmosphere through CO_2. In the third and fourth panel, we show the particle clouds for a mixing ratio of 50% CO_2 and an atmosphere that is exposed to the XUV flux values that are expected for an age of 3.7 and 3.2 Ga ago. The extent of the atmosphere and the amount of ionized particles increase significantly going back in time, which is due to a higher XUV flux and the related rapid increase in the inner boundary altitude and temperature in this time period, as shown in Figure 1. We find similar trends for the particle clouds of other CO_2 mixing ratios.

Figure 4 shows the evolution of the ion production rates of N^+, O^+ and C^+ for the assumed five CO_2 mixing ratio cases. Due to using the same atmospheric input parameters for 3.2-3.3 Ga and 3.8-3.9 Ga, as stated in Section 2.1, with the only difference being solar wind and magnetospheric parameters, the escape rates for those times are quite similar. The escape rate of all three species significantly increases going back in time, emphasizing the importance of a CO_2-rich atmosphere for early Earth as protection against excessive escape. In particular for nitrogen and carbon, a larger amount of CO_2 in the atmosphere significantly decreases the escape rate.

There are several factors influencing the behavior of the oxygen curves in Figure 4. From Table 1, we can see that atomic O densities at the inner boundary are higher for higher CO_2 mixing ratios because oxygen is produced due to the photodissociation of CO_2 molecules. For later times towards 3 Ga, the higher O densities push the oxygen escape rates up for higher CO_2 levels. On the other hand, other conditions such as increased temperature and corresponding expansion of the upper atmosphere favor escape for lower CO_2 mixing ratios. For this reason, O^+ escape for lower CO_2 mixing ratios increases once these other factors start to dominate. In addition to that, the opening of the polar angle Θ and the magnetosphere properties influence the results too. For nitrogen and carbon, the density and temperature at the inner boundary influences the escape rates mainly, but

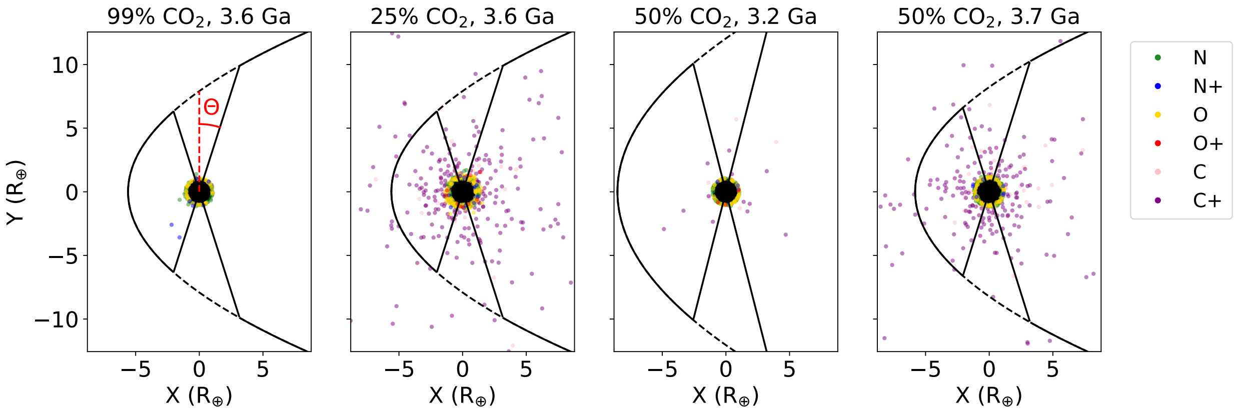

Figure 3: Particle clouds of neutral and ionized nitrogen, oxygen and carbon for different CO_2 mixing ratios and ages. We include the Earth as a filled black circle at the center with its paraboloid magnetosphere, where the dashed lines show the locations of the open field line bundle. All slices are of the same width in the z-direction ($5 \cdot 10^5$ m). Because there are far more neutrals than ions, in the interest of clarity, we only plot every 60^{th} neutral metaparticle. Due to the overabundance of carbon metaparticles, we further only plot every 5^{th} carbon metaparticle. The polar opening angle Θ is shown in red in the first panel.

for oxygen, minor changes in the opening angle of the magnetosphere provide additional jumps in the escape curves. Since there are competing factors that work in opposite directions for the ionization of oxygen, the curves lie closer together. Furthermore, the results produced by a DSMC algorithm are random by definition. When the curves lie closer, this randomness is more apparent.

In Table 3 we summarize the escape rates of ionized nitrogen ($\tau_{\text{esc,N+}}$), oxygen ($\tau_{\text{esc,O+}}$), and carbon ($\tau_{\text{esc,C+}}$) depending on the CO_2 mixing ratio and age calculated using our DSMC particle code. These escape rates reflect the ion production rates and can be interpreted as upper limits of escape through polar outflow. Furthermore, Table 4, shows the atmospheric mass lost by the different species and in total through polar outflow over the age of 3-4 Ga for 99% and 75% CO_2, 3-3.9 Ga for 50% CO_2, 3-3.7 Ga for 25% CO_2, and 3-3.4 Ga ago for 10% CO_2. The table shows the mass lost through N^+, O^+ and C^+ separately, as well as the total mass lost through all three species over the corresponding periods for each CO_2 mixing ratio. It is important to note that the mass losses cannot all be directly compared, since some were calculated over different time periods. In particular for the 10% CO_2 case, the total mass loss appears low because it was only calculated for a time period of 3-3.4 Ga ago, which is much shorter than for other CO_2 mixing ratios. From Figure 4, it is clear that lower CO_2 mixing ratios lead to more escape and that this trend would continue into the past if we had been able to simulate all CO_2 mixing ratios for earlier times as well.

CO_2	$M_{\text{loss,N+}}$ (10^{17}kg)	$M_{\text{loss,O+}}$ (10^{17}kg)	$M_{\text{loss,C+}}$ (10^{17}kg)	$M_{\text{loss,total}}$ (10^{17}kg)
99%	0.37	3.64	1.69	5.7
75%	2.78	2.94	10.12	15.84
50%	8.75	5.86	26.59	41.21
25%	19.27	2.08	16.19	37.55
10%	0.84	0.94	4.32	6.1

Table 4: Atmospheric mass lost through polar outflow of all produced ions of nitrogen ($M_{\text{loss,N+}}$), oxygen ($M_{\text{loss,O+}}$), carbon ($M_{\text{loss,C+}}$), and the total mass loss through all three species ($M_{\text{loss,total}}$). The losses are for ages 3-4 Ga ago for 99% and 75% CO_2, 3-3.9 Ga ago for 50% CO_2, 3-3.7 Ga ago for 25% CO_2, and 3-3.4 Ga ago for 10% CO_2.

Figure 5 shows the total atmospheric mass loss through polar outflow from Table 3 for each time step in age for the different CO_2 mixing ratios. For comparison, the percentage of the atmosphere that is lost in Figure 5 is compared to the present-day atmosphere mass of $M_{\text{atm}} = 5.15 \cdot 10^{18}$kg. However, we note that the atmospheric surface pressure and likely also the total mass of the atmosphere in the Archean eon may have been lower than today (Lammer et al., 2018). Other studies suggest nitrogen partial pressures at 3.3 Ga ago (Avice et al., 2018) and 3.0-3.5 Ga ago (Marty et al., 2013) having been at most similar to the present pressure, but potentially much lower than that.

Recently, Nakayama et al. (2022) developed a 1D upper atmosphere model to simulate Earth's present-day N_2-O_2-dominated atmospheres under different XUV fluxes and applied their model to Earth-like planets. We point out that one can not directly compare their results

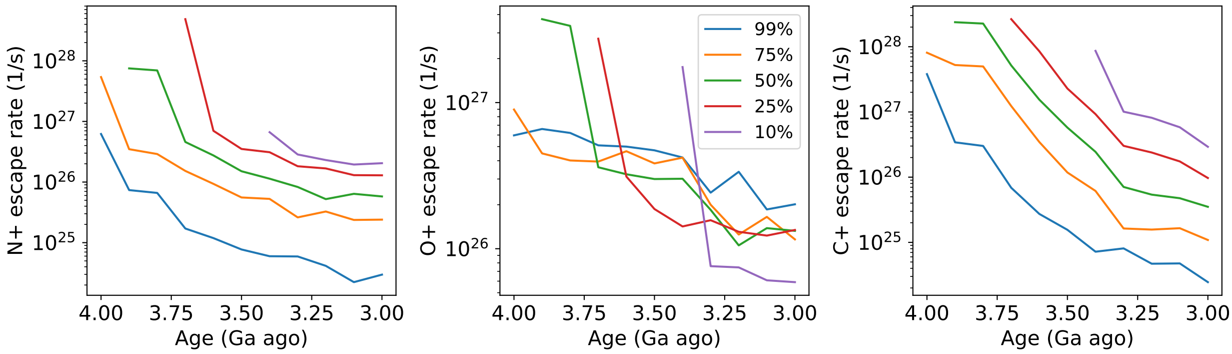

Figure 4: Evolution of ion production rates for nitrogen, oxygen, and carbon ions from 3-4 Ga, depending on the CO_2 mixing ratio. We assume these rates as a proxy for the polar escape rates of nitrogen, oxygen, and carbon.

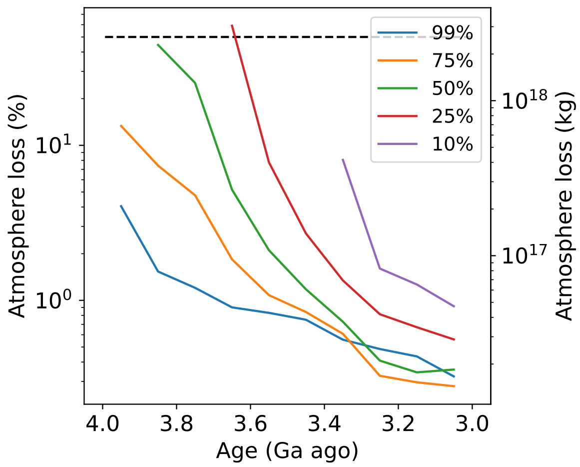

Figure 5: Total atmospheric loss between each simulated age (each time step) depending on the CO_2 mixing ratio, displayed in % of modern Earth's atmosphere mass ($M_{\mathrm{atm}} = 5.15 \cdot 10^{18}$kg) for comparison and in kilograms. The dashed black line lies at a 50% mass loss of modern Earth's atmosphere.

of the atmosphere structures to the ones we used to estimate our lower boundary densitites (Johnstone et al., 2021) because they used a very low atmosphere mixing ratio of the IR-cooling molecule CO_2 of 0.04%. Nakayama et al. (2022) suggest that atomic line cooling by oxygen prevents strong hydrodynamic expansion of and thermal loss rates from the thermosphere even for XUV fluxes up to 1000 times higher than the modern flux at the Earth's orbit. However, Nakayama et al. (2022) handle radiative transfer within their code in a simplified way by assuming that the radiation emitted through recombination processes is directly escaping into space without being reabsorbed by the atmospheric gas. On the other hand, the related cooling from radiative recombination within their theoretical model (see Fig. 5 in Nakayama et al., 2022) starts to significantly rise for 4-5 times the present-day XUV flux and even dominates the cooling for XUV fluxes higher than ~20-30 times today's XUV flux. Such cooling process, however, may be overestimated by such assumption since it is likely that more than 50% of the recombination related radiation have to be reabsorbed by the atmospheric gas below the absorption level and on the way upwards to the exosphere. This is indirectly supported by the recent non-detection of an atmosphre on the exoplanet TRAPPIST-1b by the James Webb Space Telescope (Greene et al., 2023). Therefore, the accurate efficiency of such additional oxygen cooling remains relatively unclear. Investigating its efficiency while taking into account the radiative transfer in a more realistic manner is beyond the scope of this study. Nakayama et al. (2022) also suggested that non-thermal losses like the studied ion outflow in the present study should be a dominant escape process of Earth-like atmospheres under intense XUV irradiation and solar wind exposure.

One can also summarize from our results that higher mixing ratios of the IR-cooling CO_2 is important for the reduction of non-thermal ion loss rates. It appears from Figure 5 that from 3.6-4.0 Ga ago, a CO_2 mixing ratio larger than 25% may have been necessary to avoid excessive escape via polar outflow. This is in agreement with the study done by Johnstone et al. (2021) on thermal escape, which also suggests a similar lower limit of CO_2 for times earlier than 3.6 Ga ago. In fact, Johnstone et al. (2021) find that at 3.8 Ga ago, a CO_2 mixing ratio of at least 40% may have been necessary to prevent excessive thermal escape, which is also compatible with our results. Depending on how efficiently the atmosphere could be replenished through outgassing, even higher CO_2 levels may have been necessary in the first half of the Archean. Close to 4 Ga ago, even 50% CO_2

may have been necessary due to a denser and faster solar wind. For times later than 3.5 Ga ago, lower CO_2 levels are sufficient to prevent excessive escape, which aligns well with studies indicating a steady decrease of CO_2 going towards the present (e.g., Catling and Zahnle, 2020).

There are some hints, however, that only modest amounts of nitrogen might have been lost into space over time. The present-day atmospheric $^{14}N/^{15}N$ ratio shows very low fractionation of about 40 per mille from its primordial value (e.g., Cartigny and Marty, 2013) with part of it potentially stemming from biological processes (e.g., Zerkle et al., 2017). Since atmospheric escape preferentially removes the lighter isotope from an atmosphere, isotopic fractionation can be seen as a tracer of volatile loss into space over time (see, e.g., Lammer et al., 2020, for a review). Based on such fractionation, Sproß et al. (2021) estimated that about ≤100 mbar of nitrogen could have been lost from the Earth non-thermally, in the case that the entire fractionation of $^{14}N/^{15}N$ was derived from atmospheric escape. Such a relatively low value would indicate that CO_2 mixing ratios must indeed have been relatively high (>50%) during the early Archean eon, with mixing ratios likely being above 10% for 3 Ga.

Based on raindrop imprints on an ancient shoreline, a study by Som et al. (2016) further suggests that the total surface pressure at 2.7 Ga was only around 0.23±0.23 bar, indicating that most of today's atmosphere must have built up later-on. Such low atmospheric pressure further opens the possibility that most of Earth's early atmosphere was lost during the Archeon eon. This complicates the picture, since complete loss and subsequent degassing of pristine nitrogen would mostly reset atmospheric N_2 isotope ratios. Studies by Stüeken et al. (2016) and Sproß et al. (2021) have shown that nitrogen degassing and biological recycling of NH_X and NO_X molecules back into the atmosphere as N_2 can indeed build up Earth's present-day nitrogen-dominated atmosphere after 2.7 Ga, during ages at which a nitrogen-dominated atmosphere with only modest CO_2 mixing ratios can be considered to be aeronomically stable.

A better insight into the evolution of Earth's early atmosphere prior to 2.7 Ga could be gained by precisely modeling the evolution of $^{14}N/^{15}N$ over time. Such simulations, however, are beyond the scope of the present study.

4. Conclusions

Using atmospheric profiles for the Archean Earth, we estimated the upper limits of atmospheric escape via polar outflow for 3-4 Ga ago. We find that in the early Archean, particularly for times earlier than 3.6 Ga ago, an atmosphere with a CO_2 mixing ratio of larger than 25% may have been necessary to prevent excessive polar outflow escape. Going further into the past towards 4 Ga ago, even a CO_2 mixing ratio of 50% may be necessary, depending on how efficiently the atmosphere was replenished. All in all, our work suggests relatively high CO_2 mixing ratios necessary to protect the early Earth's atmosphere, similar to the findings of other studies. In conclusion, although this work provides a quantitative estimate of the polar outflow escape rate in the Archean, further studies such as modelling $^{14}N/^{15}N$ over time will be required to constrain the necessary CO_2 mixing ratio more precisely and compare the escape rates to other sources and sinks, such as volcanic degassing and biological activity.

CRediT authorship contribution statement

Natalie Grasser performed all numerical simulations, has done the bulk of data analysis and has written most of the article's text. **Kristina Kislyakova** has created the concept of the article, has supervised the work and has written the version of the DSMC code used to estimate the polar wind escape rates. **Manuel Scherf** has provided simulations of the paleo-Earth magnetosphere and the solar wind conditions in the Archean. **Helmut Lammer** has contributed his expertise in atmospheric loss processes and evolution of the Earth's atmospheric inventory. **Gwenaël van Looveren** has performed additional upper atmosphere Kompot simulations necessary to complete the set of DSMC input parameters and contributed with his knowledge on the Kompot atmospheric model. All authors have contributed to the text.

Declaration of competing interest

The authors declare that they have no known competing financial interests or personal relationships that could have appeared to influence the work reported in this paper.

Data availability

The data is available upon request.

Acknowledgements

The authors acknowledge the support by the Austrian Research Promotion Agency (FFG) Project 873671 "SmileEarth". MS acknowledges support by the Austrian Science Fund (FWF) Project P33620. The authors are grateful to Mats Holmström for developing the original version of the DSCM code, and Maxim Khodachenko and Igor Alexeev for developing the PMM model.

References

Alexeev, I.I., 2006. Solar Wind Control of the Magnetospheric and Auroral Dynamics. 122, 55–68. doi:10.1007/s11214-006-7021-9.

Alexeev, I.I., Belenkaya, E.S., Kalegaev, V.V., Feldstein, Y.I., Grafe, A., 1996. Magnetic storms and magnetotail currents. 101, 7737–7748. doi:10.1029/95JA03509.

Alexeev, I.I., Feldstein, Y.I., 2001. Modeling of geomagnetic field during magnetic storms and comparison with observations. Journal of Atmospheric and Solar-Terrestrial Physics 63, 431–440. doi:10.1016/S1364-6826(00)00170-X.

Atkins, P., de Paula, J., 2000. Physical Chemistry for the Life Sciences.

Avice, G., Marty, B., Burgess, R., Hofmann, A., Philippot, P., Zahnle, K., Zakharov, D., 2018. Evolution of atmospheric xenon and other noble gases inferred from Archean to Paleoproterozoic rocks. 232, 82–100. doi:10.1016/j.gca.2018.04.018.

Bauer, S.J., Lammer, H., 2004. Planetary aeronomy : atmosphere environments in planetary systems.

Blackman, E.G., Tarduno, J.A., 2018. Mass, energy, and momentum capture from stellar winds by magnetized and unmagnetized planets: implications for atmospheric erosion and habitability. 481, 5146–5155. doi:10.1093/mnras/sty2640, arXiv:1801.00895.

Cartigny, P., Marty, B., 2013. Nitrogen isotopes and mantle geodynamics: The emergence of life and the atmosphere-crust-mantle connection. Elements 9, 359–366. doi:10.2113/gselements.9.5.359.

Catling, D.C., Zahnle, K.J., 2020. The Archean atmosphere. Science Advances 6, eaax1420. doi:10.1126/sciadv.aax1420.

Chamberlain, J.W., 1963. Planetary coronae and atmospheric evaporation. 11, 901–960. doi:10.1016/0032-0633(63)90122-3.

Chamberlain, J.W., Hunten, D.M., 1987. Theory of planetary atmospheres. An introduction to their physics and chemistry.. volume 36.

Charnay, B., Wolf, E.T., Marty, B., Forget, F., 2020. Is the Faint Young Sun Problem for Earth Solved? 216, 90. doi:10.1007/s11214-020-00711-9, arXiv:2006.06265.

Claire, M.W., Sheets, J., Cohen, M., Ribas, I., Meadows, V.S., Catling, D.C., 2012. The Evolution of Solar Flux from 0.1 nm to 160 μm: Quantitative Estimates for Planetary Studies. 757, 95. doi:10.1088/0004-637X/757/1/95.

Ebihara, Y., Yamada, M., Watanabe, S., Ejiri, M., 2006. Fate of outflowing suprathermal oxygen ions that originate in the polar ionosphere. Journal of Geophysical Research (Space Physics) 111, A04219. doi:10.1029/2005JA011403.

Feulner, G., 2012. The faint young Sun problem. Reviews of Geophysics 50, RG2006. doi:10.1029/2011RG000375, arXiv:1204.4449.

Fryxell, B., Olson, K., Ricker, P., Timmes, F.X., Zingale, M., Lamb, D.Q., MacNeice, P., Rosner, R., Truran, J.W., Tufo, H., 2000. FLASH: An Adaptive Mesh Hydrodynamics Code for Modeling Astrophysical Thermonuclear Flashes. 131, 273–334. doi:10.1086/317361.

Greene, T.P., Bell, T.J., Ducrot, E., Dyrek, A., Lagage, P.O., Fortney, J.J., 2023. Thermal emission from the Earth-sized exoplanet TRAPPIST-1 b using JWST. arXiv e-prints , arXiv:2303.14849doi:10.48550/arXiv.2303.14849, arXiv:2303.14849.

Gronoff, G., Arras, P., Baraka, S.M., Bell, J.M., Cessateur, G., Cohen, O., Curry, S.M., Drake, J.J., Elrod, M.K., Erwin, J.T., Garcia-Sage, K., Garraffo, C., Glocer, A., Gray Heavens, N., Lovato, K., Maggiolo, R., Parkinson, C.D., Wedlund, C.L.S., Weimer, D.R., Moore, W.B., 2020. Atmospheric Escape Processes and Planetary Atmospheric Evolution. arXiv e-prints , arXiv:2003.03231arXiv:2003.03231.

Güdel, M., 2007. The Sun in Time: Activity and Environment. Living Reviews in Solar Physics 4, 3. doi:10.12942/lrsp-2007-3, arXiv:0712.1763.

Gunell, H., Maggiolo, R., Nilsson, H., Stenberg Wieser, G., Slapak, R., Lindkvist, J., Hamrin, M., De Keyser, J., 2018. Why an intrinsic magnetic field does not protect a planet against atmospheric escape. 614, L3. doi:10.1051/0004-6361/201832934.

Holmström, M., Ekenbäck, A., Selsis, F., Penz, T., Lammer, H., Wurz, P., 2008. Energetic neutral atoms as the explanation for the high-velocity hydrogen around HD 209458b. 451, 970–972. doi:10.1038/nature06600, arXiv:0802.2764.

Huang, S.S., 1959. Occurrence of Life in the Universe. American Scientist 47, 397–402.

Javaux, E.J., 2019. Challenges in evidencing the earliest traces of life. 572, 451–460. doi:10.1038/s41586-019-1436-4.

Johnstone, C.P., Güdel, M., Brott, I., Lüftinger, T., 2015. Stellar winds on the main-sequence. II. The evolution of rotation and winds. 577, A28. doi:10.1051/0004-6361/201425301, arXiv:1503.07494.

Johnstone, C.P., Güdel, M., Lammer, H., Kislyakova, K.G., 2018. Upper atmospheres of terrestrial planets: Carbon dioxide cooling and the Earth's thermospheric evolution. 617, A107. doi:10.1051/0004-6361/201832776, arXiv:1806.06897.

Johnstone, C.P., Lammer, H., Kislyakova, K.G., Scherf, M., Güdel, M., 2021. The young Sun's XUV-activity as a constraint for lower CO_2-limits in the Earth's Archean atmosphere. Earth and Planetary Science Letters 576, 117197. doi:10.1016/j.epsl.2021.117197, arXiv:2109.01604.

Kanzaki, Y., Murakami, T., 2015. Estimates of atmospheric CO_2 in the Neoarchean-Paleoproterozoic from paleosols. 159, 190–219. doi:10.1016/j.gca.2015.03.011.

Kasting, J.F., Whitmire, D.P., Reynolds, R.T., 1993. Habitable Zones around Main Sequence Stars. 101, 108–128. doi:10.1006/icar.1993.1010.

Kislyakova, K., Johnstone, C., Scherf, M., Holmström, M., Alexeev, I., Lammer, H., Khodachenko, M., Güdel, M., 2020. Earth's polar outflow evolution from mid-Archean to present, in: European Planetary Science Congress, pp. EPSC2020–200. doi:10.5194/epsc2020-200.

Kislyakova, K.G., Holmström, M., Lammer, H., Odert, P., Khodachenko, M.L., 2014. Magnetic moment and plasma environment of HD 209458b as determined from Lyα observations. Science 346, 981–984. doi:10.1126/science.1257829, arXiv:1411.6875.

Kopparapu, R.K., Ramirez, R., Kasting, J.F., Eymet, V., Robinson, T.D., Mahadevan, S., Terrien, R.C., Domagal-Goldman, S., Meadows, V., Deshpande, R., 2013. Habitable Zones around Main-sequence Stars: New Estimates. 765,

131. doi:10.1088/0004-637X/765/2/13110.48550/arXiv.1301.6674, arXiv:1301.6674.
Lammer, H., 2013. Origin and Evolution of Planetary Atmospheres. doi:10.1007/978-3-642-32087-3.
Lammer, H., Scherf, M., Kurokawa, H., Ueno, Y., Burger, C., Maindl, T., Johnstone, C.P., Leizinger, M., Benedikt, M., Fossati, L., Kislyakova, K.G., Marty, B., Avice, G., Fegley, B., Odert, P., 2020. Loss and Fractionation of Noble Gas Isotopes and Moderately Volatile Elements from Planetary Embryos and Early Venus, Earth and Mars. 216, 74. doi:10.1007/s11214-020-00701-x, arXiv:2011.01064.
Lammer, H., Zerkle, A.L., Gebauer, S., Tosi, N., Noack, L., Scherf, M., Pilat-Lohinger, E., Güdel, M., Grenfell, J.L., Godolt, M., Nikolaou, A., 2018. Origin and evolution of the atmospheres of early Venus, Earth and Mars. 26, 2. doi:10.1007/s00159-018-0108-y.
Lichtenegger, H.I.M., Lammer, H., Grießmeier, J.M., Kulikov, Y.N., von Paris, P., Hausleitner, W., Krauss, S., Rauer, H., 2010. Aeronomical evidence for higher CO_2 levels during Earth's Hadean epoch. 210, 1–7. doi:10.1016/j.icarus.2010.06.042.
Lyons, T.W., Reinhard, C.T., Planavky, N.J., 2014. The rise of oxygen in Earth's early ocean and atmosphere. Nature 506, 307–315. doi:doi:10.1038/nature13068.
Marty, B., Zimmermann, L., Pujol, M., Burgess, R., Philippot, P., 2013. Nitrogen Isotopic Composition and Density of the Archean Atmosphere. Science 342, 101–104. doi:10.1126/science.1240971, arXiv:1405.6337.
Nakayama, A., Ikoma, M., Terada, N., 2022. Survival of Terrestrial N_2-O_2 Atmospheres in Violent XUV Environments through Efficient Atomic Line Radiative Cooling. 937, 72. doi:10.3847/1538-4357/ac86ca10.48550/arXiv.2210.01460, arXiv:2210.01460.
Newell, P.T., Sotirelis, T., Wing, S., 2010. Seasonal variations in diffuse, monoenergetic, and broadband aurora. Journal of Geophysical Research (Space Physics) 115, A03216. doi:10.1029/2009JA014805.
Schreider, A.A., Sazhneva, A.E., Varga, P., Denis, C., 2019. Evolution of the Virtual Dipole Moment in Earth's Geological History. Oceanology 59, 771–776. doi:10.1134/S0001437019050187.
Seki, K., Elphic, R.C., Hirahara, M., Terasawa, T., Mukai, T., 2001. On Atmospheric Loss of Oxygen Ions from Earth Through Magnetospheric Processes. Science 291, 1939–1941. doi:10.1126/science.1058913.
Shue, J.H., Chao, J.K., Fu, H.C., Russell, C.T., Song, P., Khurana, K.K., Singer, H.J., 1997. A new functional form to study the solar wind control of the magnetopause size and shape. 102, 9497–9512. doi:10.1029/97JA00196.
Shue, J.H., Song, P., Russell, C.T., Steinberg, J.T., Chao, J.K., Zastenker, G., Vaisberg, O.L., Kokubun, S., Singer, H.J., Detman, T.R., Kawano, H., 1998. Magnetopause location under extreme solar wind conditions. 103, 17691–17700. doi:10.1029/98JA01103.
Som, S.M., Buick, R., Hagadorn, J.W., Blake, T.S., Perreault, J.M., Harnmeijer, J.P., Catling, D.C., 2016. Earth's air pressure 2.7 billion years ago constrained to less than half of modern levels. Nature Geoscience 9, 448–451. doi:10.1038/ngeo2713.
Sproß, L., Scherf, M., Shematovich, V.I., Bisikalo, D.V., Lammer, H., 2021. Life as the Only Reason for the Existence of N_2-O_2-Dominated Atmospheres. Astronomy Reports 65, 275–296. doi:10.1134/S1063772921040077, arXiv:2103.09264.
Stüeken, E.E., Kipp, M.A., Koehler, M.C., Schwieterman, E.W., Johnson, B., Buick, R., 2016. Modeling pN_2 through Geological Time: Implications for Planetary Climates and Atmospheric Biosignatures. Astrobiology 16, 949–963. doi:10.1089/ast.2016.1537, arXiv:1612.02865.
Stüeken, E.E., Som, S.M., Claire, M., Rugheimer, S., Scherf, M., Sproß, L., Tosi, N., Ueno, Y., Lammer, H., 2020. Mission to Planet Earth: The First Two Billion Years. 216, 31. doi:10.1007/s11214-020-00652-3.
Tarduno, J.A., Cottrell, R.D., Bono, R.K., Oda, H., Davis, W.J., Fayek, M., van 't Erve, O., Nimmo, F., Huang, W., Thern, E.R., Fearn, S., Mitra, G., Smirnov, A.V., Blackman, E.G., 2020. Paleomagnetism indicates that primary magnetite in zircon records a strong Hadean geodynamo. Proceedings of the National Academy of Science 117, 2309–2318. doi:10.1073/pnas.1916553117.
Tarduno, J.A., Cottrell, R.D., Davis, W.J., Nimmo, F., Bono, R.K., 2015. A Hadean to Paleoarchean geodynamo recorded by single zircon crystals. Science 349, 521–524. doi:10.1126/science.aaa9114.
Tian, F., Kasting, J.F., Liu, H.L., Roble, R.G., 2008a. Hydrodynamic planetary thermosphere model: 1. Response of the Earth's thermosphere to extreme solar EUV conditions and the significance of adiabatic cooling. Journal of Geophysical Research (Planets) 113, E05008. doi:10.1029/2007JE002946.
Tian, F., Solomon, S.C., Qian, L., Lei, J., Roble, R.G., 2008b. Hydrodynamic planetary thermosphere model: 2. Coupling of an electron transport/energy deposition model. Journal of Geophysical Research (Planets) 113, E07005. doi:10.1029/2007JE003043.
Tu, L., Johnstone, C.P., Güdel, M., Lammer, H., 2015. The extreme ultraviolet and X-ray Sun in Time: High-energy evolutionary tracks of a solar-like star. 577, L3. doi:10.1051/0004-6361/201526146, arXiv:1504.04546.
Van Hoolst, T., Noack, L., Rivoldini, A., 2019. Exoplanet interiors and habitability. Advances in Physics 4, 1. doi:10.1080/23746149.2019.1630316.
Zerkle, A.L., Poulton, S.W., Newton, R.J., Mettam, C., Claire, M.W., Bekker, A., Junium, C.K., 2017. Onset of the aerobic nitrogen cycle during the Great Oxidation Event. 542, 465–467. doi:10.1038/nature20826.

Chapter 4

Conclusions

In summary, we used atmospheric profiles for the Archean Earth to estimate the atmospheric escape via polar outflow for 3-4 Ga ago. This was done by using a DSMC particle code that simulates the interactions between a planet's upper atmosphere and the solar wind. Assuming an N_2-CO_2 atmosphere for the Archean Earth, we investigated the effects of different CO_2 mixing ratios (99%,75%,50%,25%,10%) on escape, since CO_2 acts as a coolant in the upper atmosphere and provides protection against excessive escape. We simulate the ion production rates of atomic nitrogen, oxygen and carbon, which we use as a proxy for the upper limits of polar outflow escape.

We find that in the early Archean, particularly for times earlier than 3.6 Ga ago, an atmosphere with a CO_2 mixing ratio of larger than 25% may have been necessary to prevent excessive polar outflow escape. The escape rates of ions through polar outflow are very high for this period. An atmosphere with CO_2 levels of 25% or less risk losing an atmospheric mass equivalent to half of the modern Earth's atmosphere within a timeframe of just a few 100 million years in the early Archean. Going further into the past towards 4 Ga ago, even a CO_2 mixing ratio of 50% may be necessary. The exact numbers, however, also depend on how efficiently the atmosphere was replenished through outgassing, surface interaction or infalling volatiles from meteorites. The available data on these processes of replenishment is still very limited though, therefore it is difficult to draw a clear conclusion of the exact amount of required CO_2. However, our results are compatible with the findings of other studies that indicate similar constraints on the CO_2 levels in the Archean and pointing at only modest escape rates in Earth's early history. Going forward in time, the amount of CO_2 required for protection against escape steadily decreases, reaching levels of only a few percent.

In the context of habitability, our findings have important implications. We find that planets with a magnetic field are not necessarily protected from high escape rates. It is possible that Earth's Archean atmosphere could escape through polar outflow alone if only low levels of CO_2 are present. A planet seems to be particularly sensitive to polar outflow escape if its host star has a strong stellar wind, which is common during early evolutionary stages of Sun-like stars. Therefore, when assessing the habitability of a planet, it is important to consider all factors that might affect atmospheric escape. For one, the activity of its host star and how it might interact with the planetary magnetic field plays a significant role in escape. Furthermore, whether or not a planetary atmosphere can survive harsh conditions, such as strong stellar XUV radiation and winds, depends on the atmospheric composition. A higher level of greenhouse gases such as CO_2 seem to offer significant protection against high escape rates.

Furthermore, it is important to keep in mind that the Earth was already habitable and inhabited around 4 Ga ago, when the first life forms began to evolve. This work agrees with other studies on the Earth's possible atmospheric composition during the Archean eon, which exhibited orders of magnitude more CO_2 than today. The Archean Earth would be unrecognizable to us and would indeed be uninhabitable to many lifeforms that exist on modern Earth, yet these are exactly the conditions in which life first developed. Clearly, the definition of habitability is not limited to the conditions on Earth today. There is a wide range of possible habitable conditions that could allow for life to form. This should be kept in mind when evaluating the habitability of a planet.

All in all, our work suggests relatively high CO_2 mixing ratios necessary to protect the early Earth's atmosphere. Although this work provides a quantitative estimate of the polar outflow escape rate in the Archean, further studies such as modelling $^{14}N/^{15}N$ over time will be required to constrain the necessary CO_2 mixing ratio more precisely and compare the escape rates to other sources and sinks, such as volcanic degassing and biological activity.

Bibliography

Emmanuelle J. Javaux. Challenges in evidencing the earliest traces of life. , 572(7770): 451–460, August 2019. doi: 10.1038/s41586-019-1436-4.

David C. Catling and Kevin J. Zahnle. The Archean atmosphere. *Science Advances*, 6(9): eaax1420, February 2020. doi: 10.1126/sciadv.aax1420.

H. Lammer, J. H. Bredehöft, A. Coustenis, M. L. Khodachenko, L. Kaltenegger, O. Grasset, D. Prieur, F. Raulin, P. Ehrenfreund, M. Yamauchi, J. E. Wahlund, J. M. Grießmeier, G. Stangl, C. S. Cockell, Yu. N. Kulikov, J. L. Grenfell, and H. Rauer. What makes a planet habitable? , 17(2):181–249, June 2009. doi: 10.1007/s00159-009-0019-z.

José Cernicharo and Jacques Crovisier. Water in Space: The Water World of ISO. , 119(1-4): 29–69, August 2005. doi: 10.1007/s11214-005-8058-x.

Ramses M. Ramirez. A More Comprehensive Habitable Zone for Finding Life on Other Planets. *Geosciences*, 8(8):280, July 2018. doi: 10.3390/geosciences8080280.

Su-Shu Huang. Occurrence of Life in the Universe. *American Scientist*, 47(3):397–402, September 1959.

James F. Kasting, Daniel P. Whitmire, and Ray T. Reynolds. Habitable Zones around Main Sequence Stars. , 101(1):108–128, January 1993. doi: 10.1006/icar.1993.1010.

Ravi Kumar Kopparapu, Ramses Ramirez, James F. Kasting, Vincent Eymet, Tyler D. Robinson, Suvrath Mahadevan, Ryan C. Terrien, Shawn Domagal-Goldman, Victoria Meadows, and Rohit Deshpande. Habitable Zones around Main-sequence Stars: New Estimates. , 765 (2):131, March 2013. doi: 10.1088/0004-637X/765/2/13110.48550/arXiv.1301.6674.

Guillaume Gronoff, Phil Arras, Suleiman M Baraka, Jared M Bell, Gaël Cessateur, Ofer Cohen, Shannon M. Curry, Jeremy J Drake, Meredith K Elrod, Justin T. Erwin, Katherine Garcia-Sage, Cecilia Garraffo, Alex Glocer, Nicholas Gray Heavens, Kylie Lovato, Romain Maggiolo, Christopher D. Parkinson, Cyril L. Simon Wedlund, Daniel R Weimer, and William B. Moore. Atmospheric Escape Processes and Planetary Atmospheric Evolution. *arXiv e-prints*, art. arXiv:2003.03231, March 2020.

T. Van Hoolst, L. Noack, and A. Rivoldini. Exoplanet interiors and habitability. *Advances in Physics*, 4(1):1, 2019. doi: 10.1080/23746149.2019.1630316.

Joseph W. Chamberlain. Planetary coronae and atmospheric evaporation. , 11(8):901–960, August 1963. doi: 10.1016/0032-0633(63)90122-3.

J. W. Chamberlain and D. M. Hunten. *Theory of planetary atmospheres. An introduction to their physics and chemistry.*, volume 36. 1987.

C. P. Johnstone, M. Güdel, H. Lammer, and K. G. Kislyakova. Upper atmospheres of terrestrial planets: Carbon dioxide cooling and the Earth's thermospheric evolution. , 617:A107, Sep 2018. doi: 10.1051/0004-6361/201832776.

Colin P. Johnstone, Helmut Lammer, Kristina G. Kislyakova, Manuel Scherf, and Manuel Güdel. The young Sun's XUV-activity as a constraint for lower CO_2-limits in the Earth's Archean atmosphere. *Earth and Planetary Science Letters*, 576:117197, December 2021. doi: 10.1016/j.epsl.2021.117197.

Helmut Lammer. *Origin and Evolution of Planetary Atmospheres*. 2013. doi: 10.1007/978-3-642-32087-3.

Manuel Güdel. The Sun in Time: Activity and Environment. *Living Reviews in Solar Physics*, 4(1):3, Dec 2007. doi: 10.12942/lrsp-2007-3.

C. P. Johnstone, M. Güdel, I. Brott, and T. Lüftinger. Stellar winds on the main-sequence. II. The evolution of rotation and winds. , 577:A28, May 2015. doi: 10.1051/0004-6361/201425301.

Lin Tu, Colin P. Johnstone, Manuel Güdel, and Helmut Lammer. The extreme ultraviolet and X-ray Sun in Time: High-energy evolutionary tracks of a solar-like star. , 577:L3, May 2015. doi: 10.1051/0004-6361/201526146.

H. I. M. Lichtenegger, H. Lammer, J. M. Grießmeier, Yu. N. Kulikov, P. von Paris, W. Hausleitner, S. Krauss, and H. Rauer. Aeronomical evidence for higher CO_2 levels during Earth's Hadean epoch. , 210(1):1–7, Nov 2010. doi: 10.1016/j.icarus.2010.06.042.

Feng Tian, James F. Kasting, Han-Li Liu, and Raymond G. Roble. Hydrodynamic planetary thermosphere model: 1. Response of the Earth's thermosphere to extreme solar EUV conditions and the significance of adiabatic cooling. *Journal of Geophysical Research (Planets)*, 113(E5):E05008, May 2008a. doi: 10.1029/2007JE002946.

Feng Tian, Stanley C. Solomon, Liying Qian, Jiuhou Lei, and Raymond G. Roble. Hydrodynamic planetary thermosphere model: 2. Coupling of an electron transport/energy deposition model. *Journal of Geophysical Research (Planets)*, 113(E7):E07005, July 2008b. doi: 10.1029/2007JE003043.

Akifumi Nakayama, Masahiro Ikoma, and Naoki Terada. Survival of Terrestrial N_2-O_2 Atmospheres in Violent XUV Environments through Efficient Atomic Line Radiative Cooling. , 937(2):72, October 2022. doi: 10.3847/1538-4357/ac86ca10.48550/arXiv.2210.01460.

T. W. Lyons, C. T. Reinhard, and N. J. Planavky. The rise of oxygen in Earth's early ocean and atmosphere. *Nature*, 506:307–315, February 2014. doi: doi:10.1038/nature13068.

E. E. Stüeken, S. M. Som, M. Claire, S. Rugheimer, M. Scherf, L. Sproß, N. Tosi, Y. Ueno, and H. Lammer. Mission to Planet Earth: The First Two Billion Years. , 216(2):31, March 2020. doi: 10.1007/s11214-020-00652-3.

Yoshiki Kanzaki and Takashi Murakami. Estimates of atmospheric CO_2 in the Neoarchean-Paleoproterozoic from paleosols. , 159:190–219, June 2015. doi: 10.1016/j.gca.2015.03.011.

Mark W. Claire, John Sheets, Martin Cohen, Ignasi Ribas, Victoria S. Meadows, and David C. Catling. The Evolution of Solar Flux from 0.1 nm to 160 μm: Quantitative Estimates for Planetary Studies. , 757(1):95, Sep 2012. doi: 10.1088/0004-637X/757/1/95.

Stephen J. Mojzsis, T. Mark Harrison, and Robert T. Pidgeon. Oxygen-isotope evidence from ancient zircons for liquid water at the Earth's surface 4,300Myr ago. , 409(6817):178–181, January 2001.

L. Paul Knauth and Donald R. Lowe. High Archean climatic temperature inferred from oxygen isotope geochemistry of cherts in the 3.5 Ga Swaziland Supergroup, South Africa. *Geological Society of America Bulletin*, 115:566–580, May 2003. doi: 10.1130/0016-7606(2003)115⟨0566:HACTIF⟩2.0.CO;2.

Georg Feulner. The faint young Sun problem. *Reviews of Geophysics*, 50(2):RG2006, May 2012. doi: 10.1029/2011RG000375.

Benjamin Charnay, Eric T. Wolf, Bernard Marty, and François Forget. Is the Faint Young Sun Problem for Earth Solved? , 216(5):90, July 2020. doi: 10.1007/s11214-020-00711-9.

Eric G. Blackman and John A. Tarduno. Mass, energy, and momentum capture from stellar winds by magnetized and unmagnetized planets: implications for atmospheric erosion and habitability. , 481(4):5146–5155, Dec 2018. doi: 10.1093/mnras/sty2640.

Herbert Gunell, Romain Maggiolo, Hans Nilsson, Gabriella Stenberg Wieser, Rikard Slapak, Jesper Lindkvist, Maria Hamrin, and Johan De Keyser. Why an intrinsic magnetic field does not protect a planet against atmospheric escape. , 614:L3, Jun 2018. doi: 10.1051/0004-6361/201832934.

Kristina Kislyakova, Colin Johnstone, Manuel Scherf, Mats Holmström, Igor Alexeev, Helmut Lammer, Maxim Khodachenko, and Manuel Güdel. Earth's polar outflow evolution from mid-Archean to present. In *European Planetary Science Congress*, pages EPSC2020–200, September 2020. doi: 10.5194/epsc2020-200.

John A. Tarduno, Rory D. Cottrell, William J. Davis, Francis Nimmo, and Richard K. Bono. A Hadean to Paleoarchean geodynamo recorded by single zircon crystals. *Science*, 349(6247):521–524, Jul 2015. doi: 10.1126/science.aaa9114.

John A. Tarduno, Rory D. Cottrell, Richard K. Bono, Hirokuni Oda, William J. Davis, Mostafa Fayek, Olaf van 't Erve, Francis Nimmo, Wentao Huang, Eric R. Thern, Sebastian Fearn, Gautam Mitra, Aleksey V. Smirnov, and Eric G. Blackman. Paleomagnetism indicates that primary magnetite in zircon records a strong Hadean geodynamo. *Proceedings of the National Academy of Science*, 117(5):2309–2318, February 2020. doi: 10.1073/pnas.1916553117.

Siegfried J. Bauer and Helmut Lammer. *Planetary aeronomy : atmosphere environments in planetary systems*. 2004.

I. I. Alexeev, E. S. Belenkaya, V. V. Kalegaev, Y. I. Feldstein, and A. Grafe. Magnetic storms and magnetotail currents. , 101(A4):7737–7748, April 1996. doi: 10.1029/95JA03509.

I. I. Alexeev and Y. I. Feldstein. Modeling of geomagnetic field during magnetic storms and comparison with observations. *Journal of Atmospheric and Solar-Terrestrial Physics*, 63(5):431–440, March 2001. doi: 10.1016/S1364-6826(00)00170-X.

A. A. Schreider, A. E. Sazhneva, P. Varga, and C. Denis. Evolution of the Virtual Dipole Moment in Earth's Geological History. *Oceanology*, 59(5):771–776, September 2019. doi: 10.1134/S0001437019050187.

J. H. Shue, J. K. Chao, H. C. Fu, C. T. Russell, P. Song, K. K. Khurana, and H. J. Singer. A new functional form to study the solar wind control of the magnetopause size and shape. , 102(A5):9497–9512, May 1997. doi: 10.1029/97JA00196.

J. H. Shue, P. Song, C. T. Russell, J. T. Steinberg, J. K. Chao, G. Zastenker, O. L. Vaisberg, S. Kokubun, H. J. Singer, T. R. Detman, and H. Kawano. Magnetopause location under extreme solar wind conditions. , 103(A8):17691–17700, Aug 1998. doi: 10.1029/98JA01103.

I. I. Alexeev. Solar Wind Control of the Magnetospheric and Auroral Dynamics. , 122(1-4):55–68, Feb 2006. doi: 10.1007/s11214-006-7021-9.

P. Atkins and J. de Paula. *Physical Chemistry for the Life Sciences*. 2000.

M. Holmström, A. Ekenbäck, F. Selsis, T. Penz, H. Lammer, and P. Wurz. Energetic neutral atoms as the explanation for the high-velocity hydrogen around HD 209458b. , 451(7181):970–972, Feb 2008. doi: 10.1038/nature06600.

Alejandro L. Garcia. Direct simulation monte carlo: Theory, methods, and open challenges. 2011.

G. A. Bird. Molecular gas dynamics. *NASA STI/Recon Technical Report A*, 76:40225, January 1976.

Kristina G. Kislyakova, Mats Holmström, Helmut Lammer, Petra Odert, and Maxim L. Khodachenko. Magnetic moment and plasma environment of HD 209458b as determined from Lyα observations. *Science*, 346(6212):981–984, Nov 2014. doi: 10.1126/science.1257829.

Y. Ebihara, M. Yamada, S. Watanabe, and M. Ejiri. Fate of outflowing suprathermal oxygen ions that originate in the polar ionosphere. *Journal of Geophysical Research (Space Physics)*, 111(A4):A04219, Apr 2006. doi: 10.1029/2005JA011403.

Patrick T. Newell, Thomas Sotirelis, and Simon Wing. Seasonal variations in diffuse, monoenergetic, and broadband aurora. *Journal of Geophysical Research (Space Physics)*, 115(A3): A03216, March 2010. doi: 10.1029/2009JA014805.

B. Fryxell, K. Olson, P. Ricker, F. X. Timmes, M. Zingale, D. Q. Lamb, P. MacNeice, R. Rosner, J. W. Truran, and H. Tufo. FLASH: An Adaptive Mesh Hydrodynamics Code for Modeling Astrophysical Thermonuclear Flashes. , 131(1):273–334, November 2000. doi: 10.1086/317361.

K. Seki, R. C. Elphic, M. Hirahara, T. Terasawa, and T. Mukai. On Atmospheric Loss of Oxygen Ions from Earth Through Magnetospheric Processes. *Science*, 291(5510):1939–1941, Mar 2001. doi: 10.1126/science.1058913.

Pierre Cartigny and Bernard Marty. Nitrogen isotopes and mantle geodynamics: The emergence of life and the atmosphere-crust-mantle connection. *Elements*, 9:359–366, 10 2013. doi: 10.2113/gselements.9.5.359.